Reactive Infiltration of MORB-Eclogite-Derived Carbonated Silicate Melt into Fertile Peridotite at 3 GPa and Genesis of Alkalic Magmas

ANANYA MALLIK[1]* AND RAJDEEP DASGUPTA[1]

[1]RICE UNIVERSITY, DEPARTMENT OF EARTH SCIENCE, 6100 MAIN STREET, MS 126, HOUSTON, TX 77005, USA

We performed experiments between two different carbonated eclogite-derived melts and lherzolite at 1375°C and 3 GPa by varying the reacting melt fraction from 8 to 50 wt %. The two starting melt compositions were (1) alkalic basalt with 11·7 wt % dissolved CO_2 (ABC), (2) basaltic andesite with 2·6 wt % dissolved CO_2 (BAC). The starting melts were mixed homogeneously with peridotite to simulate porous reactive infiltration of melt in the Earth's mantle. All the experiments produced an assemblage of melt + orthopyroxene + clinopyroxene + garnet ± olivine; olivine was absent for a reacting melt fraction of 50 wt % for ABC and 40 wt % for BAC. Basanitic ABC evolved to melilitites (on a CO_2-free basis, SiO_2 ~27–39 wt %, TiO_2 ~2·8–6·3 wt %, Al_2O_3 ~4·1–9·1 wt %, FeO ~11–16 wt %, MgO ~17–21 wt %, CaO ~13–21 wt %, Na_2O ~4–7 wt %, CO_2 ~10–25 wt %) upon melt–rock reaction and the degree of alkalinity of the reacted melts is positively correlated with melt–rock ratio. On the other hand, reacted melts derived from BAC (on a CO_2-free basis SiO_2 ~42–53 wt %, TiO_2 ~6·4–8·7 wt %, Al_2O_3 ~10·5–12·3 wt %, FeO* ~6·5–10·5 wt %, MgO ~7·9–15·4 wt %, CaO ~7·3–10·3 wt %, Na_2O ~3·4–4 wt %, CO_2 ~6·2–11·7 wt %) increase in alkalinity with decreasing melt–rock ratio. We demonstrate that owing to the presence of only 0·65 wt % of CO_2 in the bulk melt–rock mixture (corresponding to 25 wt % BAC + lherzolite mixture), nephelinitic-basanite melts can be generated by partial reactive crystallization of basaltic andesite as opposed to basanites produced in volatile-free conditions. Post 20% olivine fractionation, the reacted melts derived from ABC at low to intermediate melt–rock ratios match with 20–40% of the population of natural nephelinites and melilitites in terms of SiO_2 and CaO/Al_2O_3, 60–80% in terms of TiO_2, Al_2O_3 and FeO, and <20% in terms of CaO and Na_2O. The reacted melts from BAC, at intermediate melt–rock ratios, are excellent matches for some of the Mg-rich (MgO >15 wt %) natural nephelinites in terms of SiO_2, Al_2O_3, FeO*, CaO, Na_2O and CaO/Al_2O_3. Not only can these reacted melts erupt by themselves, they can also act as metasomatizing agents in the Earth's mantle. Our study suggests that a combination of subducted, silica-saturated crust–peridotite interaction and the presence of CO_2 in the mantle source region are sufficient to produce a large range of primitive alkalic basalts. Also, mantle potential temperatures of 1330–1350°C appear sufficient to produce high-MgO, primitive basanite–nephelinite if carbonated eclogite melt and peridotite interaction is taken into account.*

INTRODUCTION

Intraplate oceanic basalts are one of the key tools to decipher mantle processes. The variability displayed in their trace element and isotopic characteristics indicates the presence of several heterogeneous domains in their source (i.e. the Earth's mantle) (Zindler & Hart, 1986; Hofmann, 1997). Because recycled, altered oceanic crust (MORB-eclogite at upper mantle conditions) has been proposed to be a major contributor to mantle heterogeneity (e.g. Hofmann, 1988, 1997; Lassiter & Hauri, 1998; Stixrude & Lithgow-Bertelloni, 2012), it is important to evaluate its role in contributing to the genesis of oceanic basalts. Based on their high $^{206}Pb/^{204}Pb$ ratio, it has been invoked that HIMU (high-μ) basalts [i.e. basalts that bear evidence of high, time-integrated $^{238}U/^{204}Pb$ (μ)] contain

*Corresponding author. E-mail: Ananya.Mallik@rice.edu

recycled oceanic crust in their source (e.g. Chase, 1981; Hofmann & White, 1982; Hofmann, 1997).

Basalts with HIMU signatures are found to be alkalic and Si-undersaturated (Kogiso et al., 1998; Jackson & Dasgupta, 2008) and the compositions of such alkalic magmas cannot simply be generated by varying the conditions of melting of mantle peridotite (Dasgupta et al., 2010). Furthermore, partial melting of a volatile-free MORB-eclogite (subducted oceanic crust) alone does not explain the genesis of such lavas, because the partial melts are dacitic to basaltic and do not contain high enough MgO and low enough SiO_2 (Yaxley & Green, 1998; Pertermann & Hirschmann, 2003; Spandler et al., 2008) to serve as primary alkalic basalts. One may argue that because low-degree partial melting of peridotite produces alkalic magmas, the contribution from recycled MORB-eclogite needs to provide only the appropriate chemical components; that is, MORB-eclogite should be responsible only for supplying the necessary chemical enrichment that drives the peridotite partial melts to match plausible primary alkali basalt compositions. However, some of those necessary vectors such as low SiO_2, low Al_2O_3, high CaO and high FeO* also cannot be derived from MORB-eclogite melting alone.

One key consideration, however, is that partial melts of MORB-eclogite, entrained in the convective mantle, are not likely to segregate and mix with peridotite partial melts or erupt unmodified. Both volatile-free and carbonate-bearing recycled oceanic crust begin to melt deeper than volatile-free peridotite (Yasuda et al., 1994; Pertermann & Hirschmann, 2003; Spandler et al., 2008), thereby creating a depth range over which MORB-eclogite-derived partial melts may interact with subsolidus peridotite. The siliceous partial melts of MORB-eclogite, not being in equilibrium with the surrounding mantle, undergo reactive crystallization (Yaxley & Green, 1998; Lambart et al., 2012; Mallik & Dasgupta, 2012). The recent study of Mallik & Dasgupta (2012) investigated such a melt–rock reaction in a volatile-free system to evaluate how an MgO-poor, siliceous partial melt of MORB-eclogite evolves upon reaction with a sub-solidus garnet lherzolite, in variable ratio, in the uppermost part of the convective mantle. At low melt–rock ratios it was observed that siliceous MORB-eclogite-derived melts evolved to alkalic basalts in the porous flow regime with many major element characteristics (high TiO_2 and CaO; low SiO_2 and Al_2O_3) similar to those of HIMU lavas; however, at the experimental pressure–temperature conditions of this study (i.e. at 3 GPa and 1375–1440°C) they were not low enough in SiO_2 and Al_2O_3 or high enough in FeO*, CaO and CaO/Al_2O_3 to explain the compositions of many naturally occurring basanites and nephelinites. Furthermore, volatile-free eclogite melt–peridotite interactions (Mallik & Dasgupta, 2012) at the base of the oceanic lithosphere

do not produce any melt compositions that are close to silica-undersaturated basalts such as melilitites or nephelinites (Le Bas, 1989).

Based on the degree of silica-undersaturation required to generate some of the alkalic basalts in general and HIMU basalts in particular, the presence of CO_2 in the source of these magmas has been proposed by many previous experimental studies (e.g. Wyllie & Huang, 1976; Eggler, 1978; Wyllie, 1978; Spera, 1981; Hirose, 1997; Dasgupta et al., 2006, 2007, 2010; Jackson & Dasgupta, 2008; Gerbode & Dasgupta, 2010). The involvement of CO_2 in the formation of silica-poor ocean island basalt (OIB) is also supported by the natural association of carbonatites, carbonate minerals, and CO_2-rich fluids and silica-poor alkalic basalts and/or mantle xenoliths and has been pointed out by many previous researchers (e.g. Dasgupta et al., 2007, and references therein)

In previous experimental studies it has been observed that the presence of CO_2 in the source reduces the SiO_2 and Al_2O_3 content and enhances the FeO*, CaO and CaO/Al_2O_3 of peridotite-derived (Hirose, 1997; Dasgupta et al., 2007) and eclogite-derived partial melts (Gerbode & Dasgupta, 2010; Kiseeva et al., 2012) when compared with their CO_2-free counterparts. Although partial melts of carbonated peridotite, by themselves, are not sufficiently enriched in TiO_2 to explain most of the alkalic ocean island basalts, partial melts of carbonated MORB-eclogite fail to explain the high MgO and low Al_2O_3 concentrations required by most HIMU alkalic basalts, basanites and nephelinites (Dasgupta et al., 2006; Gerbode & Dasgupta, 2010; Kiseeva et al., 2012; Fig. 1), which indicates the requirement of a peridotitic component (Dasgupta et al., 2007; Jackson & Dasgupta, 2008). However, although low-degree melting of carbonated, silica-excess eclogite (with coesite present in the residue) yields highly siliceous (andesitic to dacitic) melts, such melts may carry a modest concentration of dissolved CO_2 at equilibrium with immiscible carbonatitic melts (Hammouda, 2003; Kiseeva et al., 2012). Therefore, reactive infiltration of MORB-eclogite-derived partial melt into a peridotite matrix needs to be constrained not only under volatile-free conditions but also in scenarios where such reactive process takes place in the presence of CO_2, or in other words where the reacting eclogite partial melt is carbonated. Incidentally, all previous studies on partial melting of carbonated peridotite considered a direct flux of CO_2 or carbonates on the partial melting behavior not taking into account the possibility of a 'flux' in the form of dissolved CO_2 in an eclogite-derived silicate melt. The difference in the two processes of CO_2 flux to the peridotite may result in distinctly different equilibrated melt compositions; however, no systematic studies have been performed on the latter.

One of the key reactions that drive the composition of dacitic or andesitic eclogitic melt undergoing partial
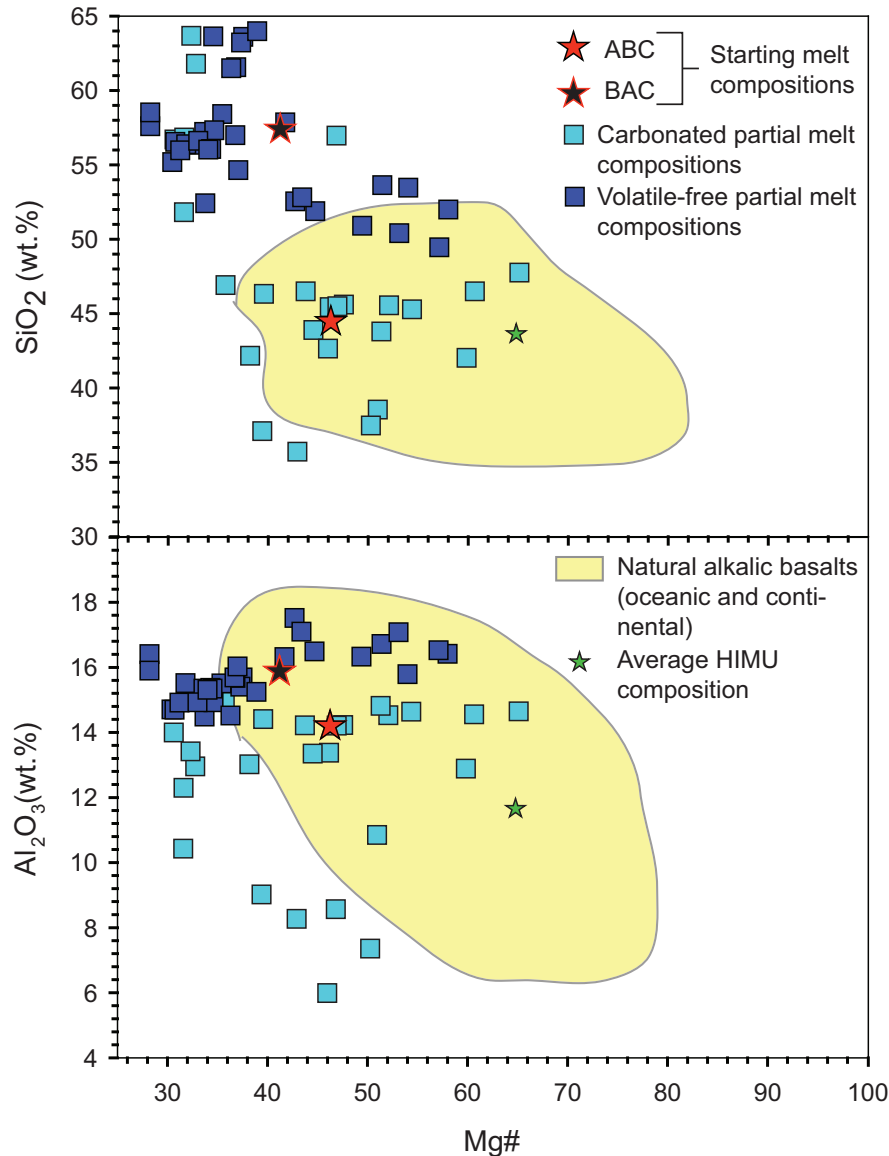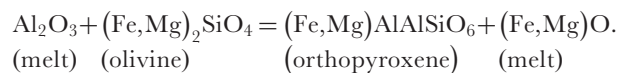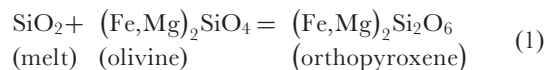
Fig. 1. $Mg\#$ vs SiO_2 (wt %) and Al_2O_3 (wt %) concentrations in starting melt compositions ABC and BAC compared with experimentally derived, volatile-free, MORB-eclogite partial melt compositions (Pertermann & Hirschmann, 2003; Spandler *et al.*, 2008) and carbonated MORB-eclogite partial melt compositions (Hammouda, 2003; Gerbode & Dasgupta, 2010; Kiseeva *et al.*, 2012), natural oceanic and continental alkalic basalts (references given in captions of Figs 12, 14 and 15) and average HIMU composition (Jackson & Dasgupta, 2008). All compositions are plotted on a volatile-free basis.

reactive crystallization in a peridotite matrix is the consumption of olivine and precipitation of orthopyroxene (Yaxley & Green, 1998; Lambart *et al.*, 2012; Mallik & Dasgupta, 2012) as follows:

$$SiO_2 + (Fe,Mg)_2SiO_4 = (Fe,Mg)_2Si_2O_6 \quad (1)$$
$$\text{(melt)} \quad \text{(olivine)} \quad\quad \text{(orthopyroxene)}$$

$$Al_2O_3 + (Fe,Mg)_2SiO_4 = (Fe,Mg)AlAlSiO_6 + (Fe,Mg)O.$$
$$\text{(melt)} \quad \text{(olivine)} \quad\quad \text{(orthopyroxene)} \quad\quad \text{(melt)}$$
$$(2)$$

The presence of CO_2 may critically affect these reactions, because it is well known from the pioneering study of Kushiro (1975) and documented by later studies by Brey & Green (1975, 1977) that the stability of orthopyroxene is enhanced at the expense of olivine at the liquidus of primary basaltic melts. Thus, one may expect that the presence of CO_2 would cause enhanced crystallization of orthopyroxene at the expense of olivine, driving the reacted melt towards a more silica-depleted composition as compared with its CO_2-free counterpart. Similarly, comparison of 3 GPa melting reactions of CO_2-free

peridotite partial melting (Walter, 1998) with those of CO_2-present peridotite partial melting (Dasgupta *et al.*, 2007) suggests that garnet stability is enhanced in a carbonated system. If a similar effect is applicable during reactive crystallization of MORB-eclogite melt in lherzolite, then the reacted melt may achieve a more alumina-depleted composition through enhanced stability of garnet and thus become a better candidate for primary alkalic basalts. Hence the effect of CO_2 during reactive infiltration of siliceous MORB-melts into fertile peridotite could be critical in generating many of the major element geochemical features of strongly alkalic basalts. Nevertheless, the phase equilibria of reactive infiltration of MORB-eclogite-derived carbonated partial melt into a peridotitic medium are unconstrained.

In this study we investigate the fate of MORB-eclogite-derived, carbonated, partial melt upon reaction with volatile-free subsolidus, fertile peridotite in the uppermost part of the convective mantle (base of the lithosphere). The experiments were performed at the same pressure–temperature conditions as the recent study by Mallik & Dasgupta (2012), to understand directly the effect of CO_2 in such a melt–rock reaction scenario. We demonstrate that infiltration of MORB-eclogite-derived, andesitic to mildly alkalic carbonated basalts into peridotite causes the reacted melts to evolve to nephelinitic-basanite to melilititic compositions through crystallization of orthopyroxene and garnet. We also show that such reacted melt compositions are a better match for natural nephelinites, nephelinitic basanites, and melilitites from oceanic and continental provinces as compared with partial melts of carbonated eclogite and carbonated peridotite, as well as melts that are the product of reaction between a partial melt of MORB-eclogite and subsolidus peridotite in a volatile-free system.

EXPERIMENTAL TECHNIQUES
Starting materials

The MORB-eclogite-derived carbonated melts used in the reaction couple with volatile-free, fertile peridotite are (1) 'ABC', which is an alkalic basalt similar to a 43% partial melt of carbonated MORB-eclogite G2C used by Gerbode & Dasgupta (2010) and contains 11·7 wt % CO_2, and (2) 'BAC', which is a basaltic andesite with a similar composition to G2PM1 used by Mallik & Dasgupta (2012), when normalized on a volatile-free basis. BAC corresponds to 8·9 wt % partial melt of natural volatile-free MORB-eclogite G2 (Pertermann & Hirschmann, 2003) and contains 2·6 wt % of CO_2 (Table 1). The CO_2 concentrations mentioned above are based on the proportions in which oxides and carbonates were mixed to synthesize the starting melts. Both starting melt compositions lie within the range of MORB-eclogite ($\pm$ carbonates) derived partial melts produced experimentally in previous studies

Table 1: Compositions of starting materials

	Peridotite		Starting melts		
	KLB-1ox	MixKLB-1[1]	ABC	BAC	G2PM1[2]
SiO_2	44·82	44·54	44·22	56·46	56·3(8)
TiO_2	0·15	0·21	2·87	5·66	5·65(8)
Al_2O_3	3·51	3·70	13·45	15·61	15·6(4)
Cr_2O_3	0·32	0·23	0·05	0·01	0·01(1)
FeO*	8·19	8·08	15·28	8·17	8·2(3)
MnO	0·12	0·14	0·33	0·09	0·08(2)
MgO	39·50	39·30	6·87	2·51	2·5(1)
CaO	3·07	3·52	12·38	7·50	7·5(2)
Na_2O	0·30	0·29	4·21	3·76	4·02(9)
K_2O	0·02	0·01	0·33	0·21	0·21(1)
Mg#	89·58	89·66	44·50	35·42	35·4(9)
CO_2	—	—	11·7	2·6	—
Sum	100·00	100·02	100·00	100·00	99·99

Major element compositions of KLB-1ox, ABC and BAC and CO_2 concentrations based on proportions of oxides and carbonates mixed in the starting compositions. Oxide concentrations of ABC and BAC are reported on a CO_2-free basis.
*All Fe assumed to be FeO.
[1]Composition of fertile peridotite as used by Mallik & Dasgupta (2012).
[2]Composition of MORB-eclogite partial melt as used by Mallik & Dasgupta (2012).

(Fig. 1). Volatile-free peridotite KLB-1ox used in this study is similar to the fertile peridotite composition MixKLB-1 used by Mallik & Dasgupta (2012) and, within 1σ error, similar to the KLB-1 peridotite composition of Herzberg *et al.* (1990) and Davis *et al.* (2009). All starting compositions used in this study are reported in Table 1.

All the starting materials (carbonated melts and peridotite) were synthesized using high-purity oxides and carbonates from Alfa Aesar. SiO_2, TiO_2, Al_2O_3 and MgO were fired overnight at 1000°C, Fe_2O_3 at 800°C, MnO_2 at 400°C, $MgCO_3$ at 200°C, $CaCO_3$ at 250°C, and Na_2CO_3 and K_2CO_3 at 110°C to minimize adsorbed water. CO_2 was added to ABC as $MgCO_3$, $CaCO_3$, Na_2CO_3 and K_2CO_3. To maintain the desired proportion of Mg:CO_2 in this melt, Mg was added partly as MgO and the rest as $MgCO_3$. Reagent grade $MgCO_3$ often contains variable amounts of water, especially in the form of brucite. To ensure that addition of $MgCO_3$ does not introduce water in our ABC melt mix, X-ray diffraction of the fired $MgCO_3$ powder was performed, which yielded no discernible peaks for $Mg(OH)_2$. In the case of BAC, CO_2 was added only as Na_2CO_3. Prior to adding carbonates to introduce CO_2, the oxides and carbonates were ground together under ethanol in an agate mortar for 30 min. Once

the ethanol evaporated, the mixtures were fired at $1000°C$ in a $CO–CO_2$ mixing furnace at log $fO_2 \sim QFM$ -2 (where QFM is the quartz–fayalite–magnetite buffer) for 24 h to convert all the Fe^{3+} to Fe^{2+} as well as to decarbonate the powders. Once reduction was complete, carbonates were added in the case of ABC and BAC to introduce CO_2 into the starting melt mixes. The final mixtures were ground in an agate mortar under ethanol for 30 min. All starting mixtures were stored at $110°C$ to prevent adsorption of moisture at any time. The starting materials composed of 8–50 wt % carbonated eclogite-derived melt (ABC or BAC), mixed homogeneously with peridotite, simulate reactive infiltration of eclogite melt into peridotite via porous flow. The bulk CO_2 content ranged from 0·93 to 5·83 wt % for experiments with KLB-1 +ABC mixtures and from 0·21 to 1·3 wt % for experiments with KLB-1 +BAC mixtures.

Experimental procedure

The experiments were performed using end-loaded piston cylinders at Rice University using a half-inch assembly comprising $BaCO_3$ pressure medium, straight graphite furnace, crushable MgO spacers, and Pt–graphite double capsules. Pressure–temperature calibrations relevant for our experimental set-up have been given by Tsuno & Dasgupta (2011). The homogeneous mixtures were loaded into thick graphite capsules surrounded by outer platinum capsules. Before the platinum capsules were welded shut, the loaded capsules were kept at $110°C$ overnight to remove any moisture and ensure the least water contamination possible. The loss in weight of the capsules after welding was measured and in no case was the loss observed greater than 0·3% relative. The experiments were performed at $1375°C$, 3 GPa; that is, at pressure–temperature conditions equivalent to the base of mature oceanic lithosphere where the eclogite-derived carbonated melts would be above their respective liquidi but the peridotite would be below its solidus. In all the experiments, the pressure was first raised to 3 GPa and then the system was heated to $1375°C$ at $100°C\ min^{-1}$. Temperatures of the experiments were controlled and monitored using $W_{95}Re_5/W_{74}Re_{26}$ (Type C) thermocouples. The run durations varied from 47 to 172 h. Experiments were quenched by cutting off power from the heater after which the runs were decompressed slowly, the position of the capsule and thermocouple with respect to the hotspot was checked, and the capsules were recovered. The capsules were then mounted in epoxy and polished using silicon-carbide paper (240–600 grit) and polycrystalline diamond powder (diameter varying from 3 to 0·25 μm) on nylon and velvet cloths. In all circumstances, polishing was carried out in the absence of water or any lubricating liquid to preserve quench carbonate crystals expected to be present in the reacted melt pool.

Oxygen fugacities of the melt–rock reaction experiments were calculated using the calibration of Stagno & Frost

(2010) for the graphite–carbonate–oxygen buffer; these varied from QFM -1·8 to QFM -2·3, which is in agreement with the predictions of Frost & Wood (1995) and Medard et al. (2008) for experiments performed in graphite capsules. The calculated fO_2 values also lie within the range of oxygen fugacity estimates (QFM +1·5 to −3·5) for oceanic and abyssal peridotites compiled by Foley (2011).

Experimental conditions are reported in Table 2.

Analysis of run products

Analyses of textures and phase compositions were performed using a Cameca SX50 electron microprobe at Texas A&M University. High-resolution imaging was performed using an FEI Quanta 400 FEG-SEM at Rice University. Phases were identified using Imix Princeton Gamma Tech (PGT) energy-dispersive spectroscopy and reported phase compositions were determined using wavelength-dispersive spectroscopy. Although all the phases were analyzed at an accelerating voltage of 15 kV, glasses were analyzed under a beam current and diameter of 10 nA and 5–10 μm, respectively; all other phases except quench aggregates in melt pool (olivine, orthopyroxene, clinopyroxene and garnet) were analyzed using a beam current and diameter of 20 nA and 1 μm, respectively. In all the experiments, the reacted melt quenched to a heterogeneous assemblage (except for a few experiments where some of the melt formed glass pools). A large beam size of 20–30 μm and current of 20 nA were used to obtain the average composition of these heterogeneous aggregates and many such points across two to three exposed sections were analyzed to obtain a reliable mean composition of the reacted melt. No filtering technique was applied to the heterogeneous quench aggregate compositions to avoid any selective bias. Counting times for the elements analysed varied from 20 to 80 s on the peak and half the time on each background. Na was analyzed first on a given spectrometer and for only 20 s on the peak and 10 s on each background to limit its loss. Compositional zoning was observed in some garnets and in such cases, the rim compositions were analyzed assuming that the rim is in equilibrium with the rest of the assemblage. The natural mineral and basaltic standards used for phase composition analysis are the same as those used by Mallik & Dasgupta (2012). For some quench aggregate analyses, Ca and Mg concentrations were measured using a dolomite standard. However, it was found that these analyses were no different from those where the same elements were measured using a diopside standard, as in the study of Mallik & Dasgupta (2012), thereby suggesting no particular advantage of using carbonate standards over silicate standards for measuring major element cation concentrations in carbonated silicate melts.

Phase proportions for each experiment were calculated based on mass balance of components using the optimization tool Solver in MS-Excel. Minor elements such as

Table 2: Summary of melt–rock reaction experiments performed in this study including experimental conditions, phases present, and their mass proportions

Run no.	Starting materials used	Reacting melt mass (wt %)	T (°C)	T_{BKN} (°C)	T_{R00} (°C)	P (GPa)	Duration (h)	Mineral modes (wt %)					Σr^2
								Ol	Opx	Cpx	Gt	Melt	
G209*	ABC + KLB-1ox	8	1375	1332	1295	3	119	51(1)	13(1)	18(1)	13(0)	4	0·5(2)
G217†	ABC + KLB-1ox	15	1375	1350	1298	3	144	40(2)	26(3)	13(3)	13(1)	9(2)	0·6(2)
G239	ABC + KLB-1ox	25	1375	1327	1319	3	96	30(3)	28(5)	13(3)	13(1)	15(4)	0·3(1)
G240	ABC + KLB-1ox	33	1375	1323	1313	3	96	27(2)	23(4)	16(2)	14(1)	20(3)	2·0(1)
G227†	ABC + KLB-1ox	40	1375	1328	1293	3	116	22(3)	25(5)	12(2)	20(0)	21(5)	0·20(3)
G229	ABC + KLB-1ox	50	1375	1349	1301	3	93	—	40(2)	15(4)	24(1)	21(2)	0·53(9)
B126*	BAC + KLB-1ox	8	1375	1334	1276	3	95	42(1)	27(1)	14(1)	12(0)	3	0·7(4)
B157*	BAC + KLB-1ox	15	1375	1357	1314	3	100	36(1)	24(1)	17(1)	14(1)	6	0·8(3)
B222	BAC + KLB-1ox	25	1375	1340	1483	3	92	23(1)	43(1)	8(1)	7(1)	18(2)	0·2(2)
B223	BAC + KLB-1ox	33	1375	1325	1404	3	139	16(1)	43(2)	12(1)	11(1)	17(2)	0·27(6)
G231	BAC + KLB-1ox	40	1375	1378	1281	3	90	—	52(1)	20(4)	18(1)	11(2)	2(1)
G226	BAC + KLB-1ox	50	1375	1399	1308	3	115	—	33(3)	28(5)	15(1)	24(3)	3·7(6)

*Experiments where melt mass proportions are calculated by the method of linear extrapolation (equations of extrapolation are given in the caption of Fig. 3).
†Experiments re-reported from Dasgupta *et al.* (2013).
The $\pm 1\sigma$ errors, based on replicate electron microprobe analyses, are given in parentheses and reported as the least digits cited. For example, 51(1) should be read as 51 ± 1 wt %. ABC and BAC are 11·6 and 2·6 wt % CO_2-bearing starting melts, respectively and KLB-1ox is the oxide mixture used as fertile peridotite. T_{BKN} (°C), temperature obtained using the two-pyroxene thermometer of Brey & Kohler (1990); T_{R00} (°C), temperature obtained using the garnet–clinopyroxene thermometer of Ravna (2000) using average pyroxene and garnet compositions reported in Tables 5, 6 and 7; Ol, olivine; Opx, orthopyroxene; Cpx, clinopyroxene; Gt, garnet; Σr^2, sum of residual squares obtained using phase proportions, phase compositions, and the bulk starting composition; —, absence of a phase.

Cr_2O_3, MnO and K_2O, as well as CO_2, were neglected in the mass balance. The phase proportions obtained from mass balance were verified texturally to ensure their validity. Based on mass balance of FeO in the melt–rock systems, we concluded that there was no Fe loss to the outer Pt capsule.

CO_2 concentrations in the reacted melt are estimated in two ways: (1) by difference between 100% and the microprobe totals of the averaged composition of the quench aggregates (assuming all of the deficit is attributable to CO_2; hereafter referred to as 'CO_2 by difference'); (2) from modal proportions of melt by allotting the bulk CO_2 concentration to reacted melt because no solid carbonates or CO_2-rich fluid phase was present after melt–rock reaction and because carbon solubility in nominally C-free mantle silicates is negligible (Shcheka *et al.*, 2006). Both estimates are included in Table 3 and plotted in Supplementary Data Fig. S1 (available for downloading at http://www.petrology.oxfordjournals.org). Given the large uncertainty in the estimated CO_2 contents of the melts, a positive correlation between the two suggests that the trend in melt composition evolution remains unaffected by whichever method of CO_2 estimation in the reacted melts is adopted.

Because it has been demonstrated that averaging quench aggregates produces reliable estimates of melt compositions by comparison with the compositions of glassy patches, CO_2 estimates obtained 'by difference' have been used to calculate the volatile-free melt compositions reported in Table 3.

EXPERIMENTAL RESULTS
Experimental conditions and phase proportions are reported in Table 2. Photomicrographs of the run products are shown in Fig. 2. Modal proportions and mineral compositions are plotted as a function of reacting melt mass in Figs 3–8 and listed in Tables 3–7.

Textures and phase assemblages
MixKLB-1 at 3 GPa and 1375°C produced a four-phase lherzolite with olivine, orthopyroxene, clinopyroxene and garnet as described by Mallik & Dasgupta (2012). All experiments with peridotite–basaltic andesite (BAC) and peridotite–alkali basalt (ABC) mixtures produced an assemblage of orthopyroxene + clinopyroxene + garnet + melt ± olivine. In the case of 8 wt % melt-added

Table 3: Composition of reacted melts

Run no.:	G217	G239	G240	G227	G229	B222	B223	G231	G231gl	G226	G226 gl
Starting melt:	ABC	ABC	ABC	ABC	ABC	BAC	BAC	BAC	BAC	BAC	BAC
Melt added (wt %)	15	25	33	40	50	25	33	40	40	50	50
n:	26	23	18	18	50	23	18	21	32	60	60
SiO_2	30(4)	39(3)	38(2)	31(5)	27(6)	42(2)	47·3(1)	52(1)	51·5(6)	53(1)	53·2(6)
TiO_2	6·3(9)	2·8(7)	3·4(2)	4·6(8)	5(1)	6·4(4)	5·9(2)	7·0(2)	7·0(2)	8·7(3)	8·34(9)
Al_2O_3	5·2(8)	8·4(5)	9·1(5)	5·3(8)	4·1(8)	10·5(5)	11·9(4)	12·9(3)	12·7(2)	12·3(2)	12·3(1)
Cr_2O_3	0·8(6)	0·13(4)	0·10(4)	0·2(3)	0·0(4)	0·2(1)	0·2(2)	0·04(1)	0·04(2)	0·1(1)	0·05(1)
FeO*	14(2)	11(1)	12·3(9)	15(2)	16(2)	10(1)	9·9(9)	7·7(4)	7·6(2)	6·5(5)	6·35(3)
MnO	0·21(3)	0·15(2)	0·17(2)	0·22(3)	0·23(4)	0·12(3)	0·11(3)	0·05(1)	0·06(1)	0·06(1)	0·064(8)
MgO	21(2)	20·3(8)	17·2(9)	19(1)	20(1)	15·4(7)	12·2(8)	8·3(8)	9·1(5)	7·9(8)	8·6(3)
CaO	18(5)	14(2)	13(1)	20(5)	21(3)	10(1)	7·9(3)	8·7(6)	9·0(3)	7·3(4)	7·6(2)
Na_2O	4(2)	4(1)	6(2)	4(2)	7(3)	4·0(7)	4·2(4)	3·0(3)	2·9(2)	3·4(3)	3·1(4)
K_2O	0·23(1)	0·11(6)	0·21(5)	0·3(2)	0·4(2)	0·4(1)	0·34(5)	0·18(6)	0·14(2)	0·35(9)	0·31(4)
Sum	100·00	100·00	100·00	100·00	100·00	100·00	100·00	100·00	100·00	100·00	100·00
Mg#	73(9)	73(3)	69(4)	70(6)	69(4)	73(3)	69(2)	66(9)	68(4)	68(9)	71(3)
CO_2[1]	22(5)	12(3)	10(3)	23(5)	25(3)	12(6)	4(2)	7(3)	7(1)	6(2)	7·2(3)
TiO_2[2]	3·4(6)	2·8(4)	3·2(3)	3·5(5)	4·7(4)	6·0(5)	7·0(4)	12(3)	12(3)	9(1)	9(1)
Na_2O[2]	5·2(8)	4·8(8)	5·7(7)	6(1)	7·8(7)	4·5(4)	5·5(3)	5·4(7)	5·4(7)	4·0(5)	4·0(5)
K_2O[2]	0·5(1)	0·36(9)	0·34(5)	0·38(8)	0·82(9)	0·37(4)	0·23(2)	0·9(3)	0·9(3)	0·21(5)	0·21(5)
CO_2[2]	15(4)	17(3)	19(1)	23(3)	20(2)	4(2)	5·1(6)	5·8(7)	7(1)	4·0(1)	7·2(3)

*All Fe assumed to be FeO.
[1]CO_2 concentration determined by difference.
[2]TiO_2, Na_2O, K_2O and CO_2 concentrations determined from mass balance (refer to text for details).
All oxide concentrations are reported in weight per cent and on a CO_2-free basis.

experiments for both starting melt compositions and l5 wt % BAC-added experiment, no melt pool, separated as a layer, coexisting with the residual four-phase lherzolitic assemblage, was observed. In these experiments, melt was found only as pockets in triple-grain junctions (Fig. 2c). For higher melt-added experiments, a distinct melt pool composed of heterogeneous quench crystals was observed in coexistence with lherzolitic phases, except for the 40 wt % BAC-added experiment and 50 wt % ABC- and BAC-added experiments, where olivine was absent. The quenched melt pools are composed of quench clinopyroxene-like silicates intimately associated with Ca–Na–Fe carbonates (Fig. 2a, b and d). No textural evidence of a separate CO_2-rich vapor phase was observed. This is in keeping with CO_2 solubilities for silica-undersaturated melts (similar to those obtained in this study) determined by previous studies (e.g. Mysen *et al.*, 1975; Brooker, 1998; Brooker *et al.*, 2001) being similar to or exceeding the CO_2 concentrations determined for the reacted melts from this study.

In our experiments, it is observed that there is a broad linear correlation between reacting melt mass and mass fraction of melt after melt–rock reaction (Fig. 3). For the experiments with melt present only at triple junctions, melt modal proportions were estimated by linear extrapolation of the trend of modal proportions of melt as a function of amount of melt added to the experiments. Overall the melt mass increased from 4 wt % (where melt is concentrated only in triple-grain junctions) to 2l wt % for experiments with ABC and from 3·1 to 24 wt % for experiments with BAC. It is observed that the olivine mass fraction decreases from 60 wt % in the starting peridotite to 0 wt % when 50 wt % of ABC and 40 wt % of BAC are added, respectively. Olivine is consumed because of pyroxene crystallization. Accordingly, the orthopyroxene mode overall increases from l4 to 40 wt % as a result of addition of 0–50 wt % ABC. It increases from 28 to 52 wt % until 40 wt % BAC is added, followed by a decrease to 33 wt % of orthopyroxene when 50 wt % BAC is added. This decrease in orthopyroxene modal proportion between 40 and 50 wt % BAC-added experiments is compensated by an increase in clinopyroxene mode from 20 to 29 wt % over the same range of conditions. This reversal in pyroxene stabilization can be explained by an increase in bulk Ca/Mg with increasing melt added (from 0·14 for 40% BAC-added to 0·18 for 50% BAC-added
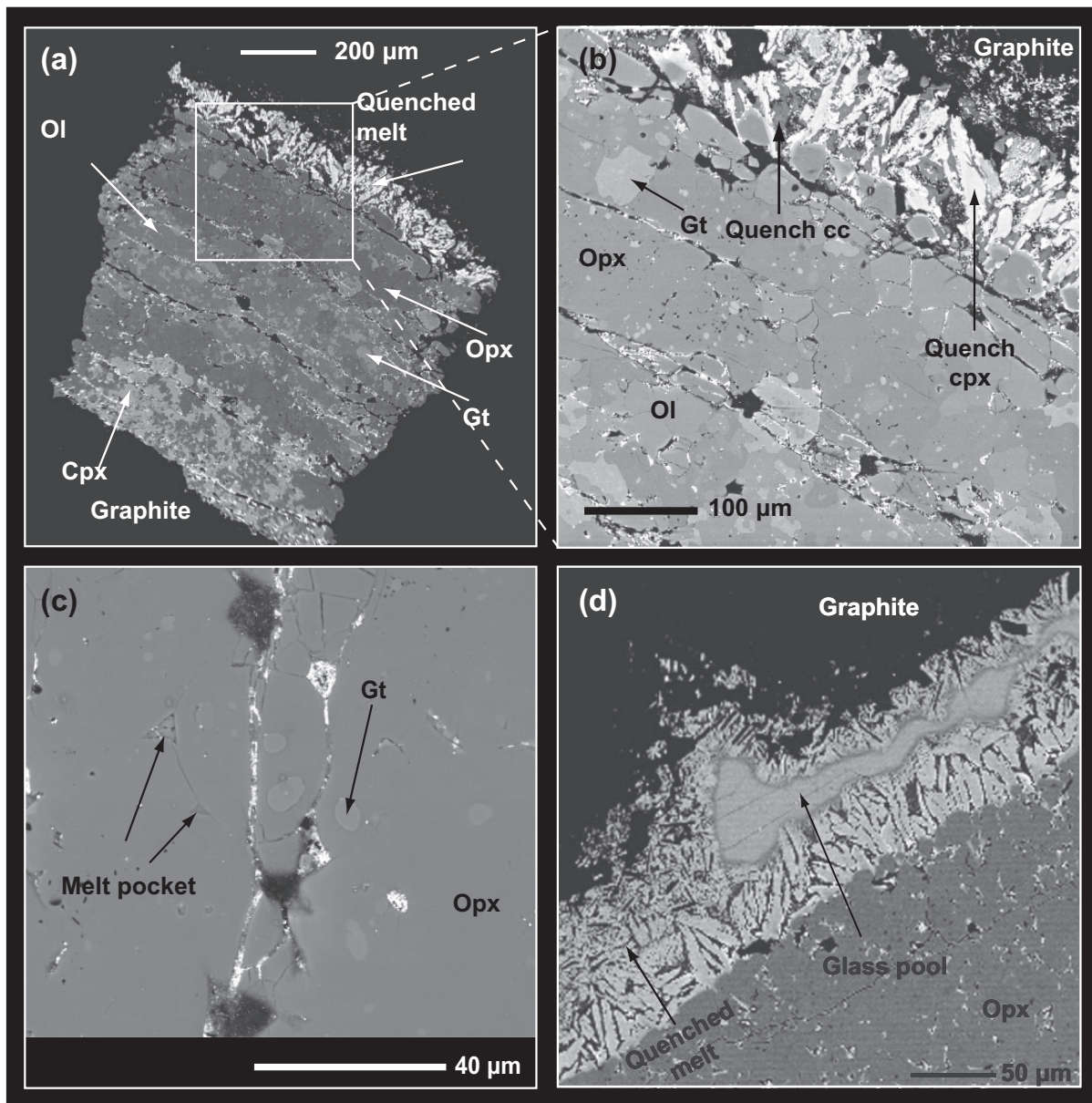
Fig. 2. Back-scattered electron images of experiments with (a) 15 wt % ABC + KLB-1 mixture (G217). Quenched melt pool is observed to co-exist with olivine, orthopyroxene, clinopyroxene and garnet in the residue. The white box represents the area that is shown magnified in (b). (b) Magnification of the area marked by white box in (a). The quench aggregates comprise clinopyroxene-like silicates and Ca–Fe–Na carbonates. (c) Melt quenched in the triple junction of orthopyroxene crystals in the residue of melt–rock reaction (G209). The melt does not form a separate pool in this experiment unlike in (a). (d) Glass pool formed along with quenched dendritic aggregate in 40 wt % BAC + KLB-1ox experiment (G231). The similarity in glass and averaged quench melt pool compositions (Fig. 4) demonstrates the reliability of our averaging technique used to measure quench melt pool compositions.

experiments). For ABC-added experiments, clinopyroxene mode displays an overall decrease from 19 to 15 wt % for 0–50 wt % melt-added runs. For BAC-added experiments, the clinopyroxene mode increases sharply from 8 to 28 wt % for added melt fraction of 25–50 wt %. Garnet modal proportions display an overall increase from 10 to 24 wt % for experiments with ABC and to 15 wt % for

experiments with BAC for the initial melt mass increasing from 0 to 50 wt % (Fig. 3).

Assessment of chemical equilibrium

The experiments in this study have not been reversed. Garnets are zoned in some instances, even though the cores are less than 1% in volume with respect to the
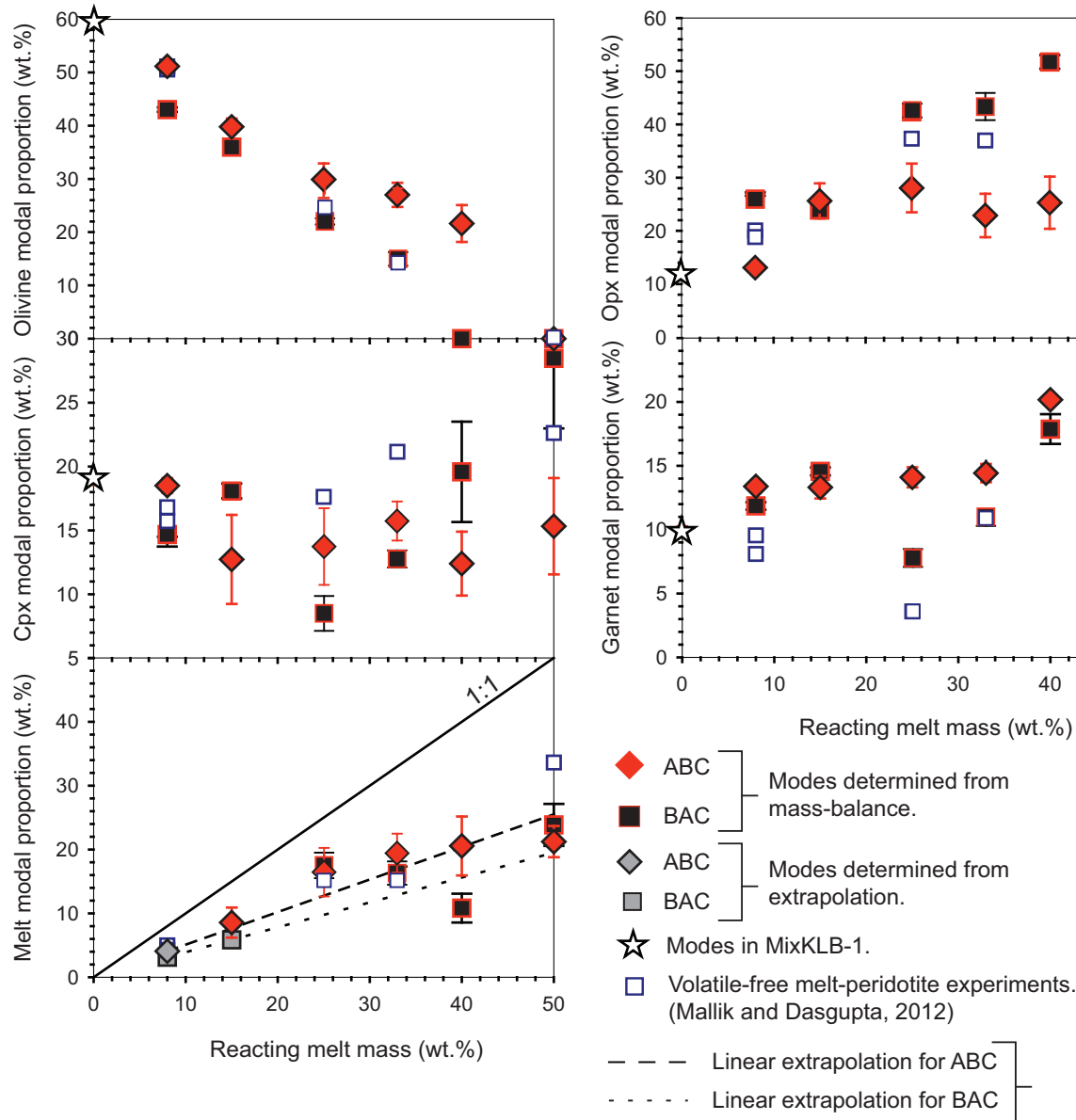
Fig. 3. Mass fractions (in wt %) of olivine, orthopyroxene (opx), clinopyroxene (cpx), garnet, and melt plotted as a function of the initial melt mass (in wt %) reacted with peridotite for experiments with two starting melts—ABC (diamonds) and BAC (filled squares). Also plotted for comparison are the fraction of reacted melts from volatile-free G2PM1 +MixKLB-1 mixtures performed at 1375°C, 3 GPa from Mallik & Dasgupta (2012) (open squares). Because no reacted melt pool was observed for the 8 wt % ABC-added run, and 8 wt % and 15 wt % BAC-added experiments, the melt fractions for these experiments were estimated by linear extrapolation of melt consumption trends constructed for ABC- and BAC-added experiments. The extrapolated melt proportions are plotted with gray symbols and the equations used are: (final melt fraction) = 0·51 × (reacting melt fraction) for ABC + KLB-lox experiments and (final melt fraction) = 0·45 × (reacting melt fraction) for BAC + KLB-lox experiments. The 1:1 line represents the locus of all points for which the mass fraction of melt added and the resulting melt fractions are the same. Error bars ($\pm 1\sigma$ wt %) are derived from mass balance calculations by propagating compositional uncertainties based on replicate microprobe analyses.

entire volume of garnet, rendering them insignificant for affecting mass balance or overall mineralogy in the experiments. Thus, even though complete equilibration has not been achieved, an approach to equilibrium and maintenance of a closed system during the experiments can be demonstrated by the following characteristics.

(1) The sum of residual squares (Σr^2; Table 2) for the carbonated melt–rock reaction experiments varies from 0·2 to two. Given the uncertainty in analyses of melt composition from averaging the heterogeneous quench phases, the experiments can be considered to have been closed to material exchange.
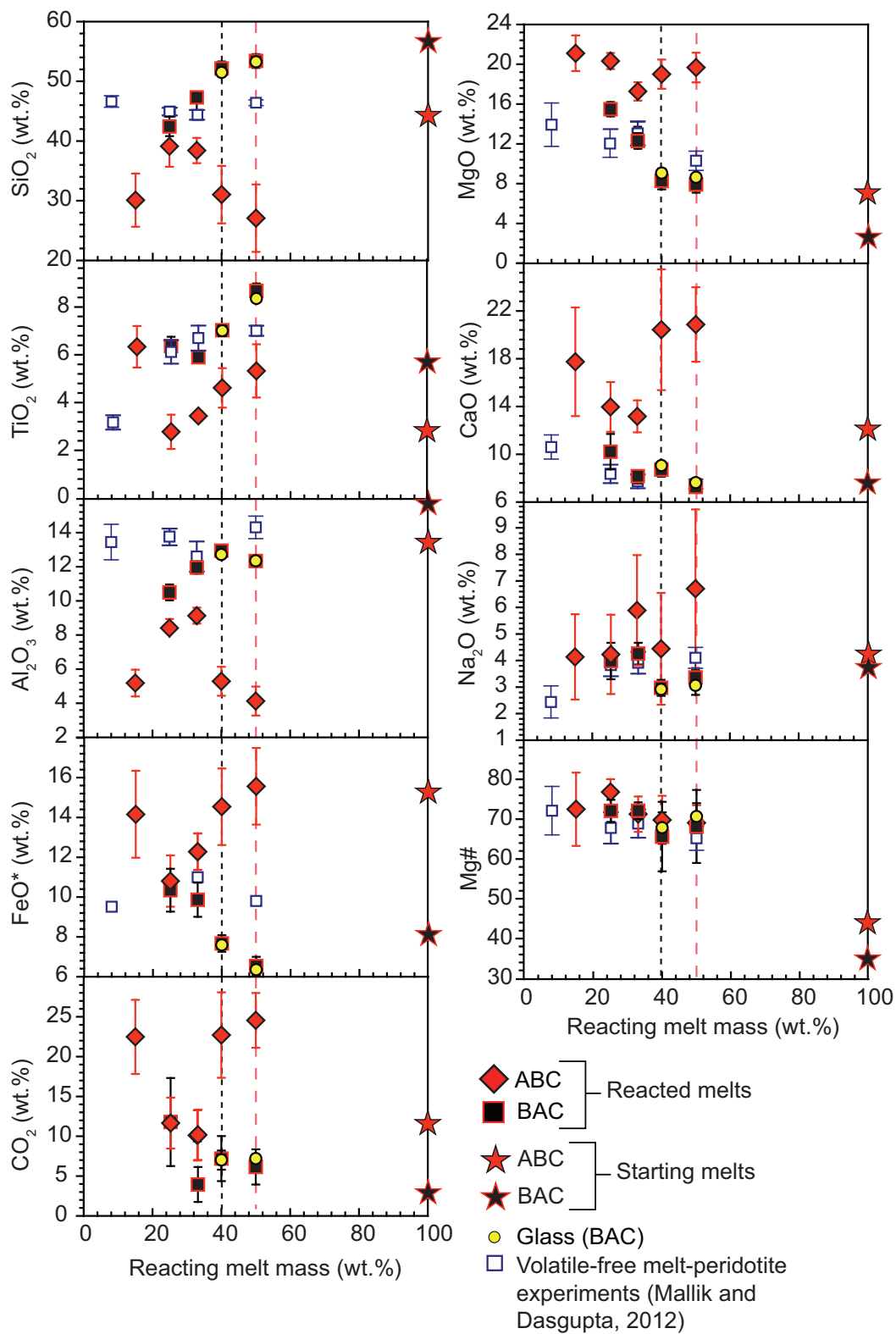
Fig. 4. Average compositions of reacted melts derived from ABC-added (diamonds) and BAC-added (filled squares) experiments plotted as a function of reacting melt mass. Plotted for comparison are the starting melt compositions ABC and BAC. The reacted melt compositions for 8 wt % ABC-added, 8 wt % and 15 wt % BAC-added experiments could not be determined owing to the absence of a quench or glass pool and the fact that the melt pockets at triple-grain junctions (Fig. 2c) were not large enough to be analyzed reliably by microprobe. For
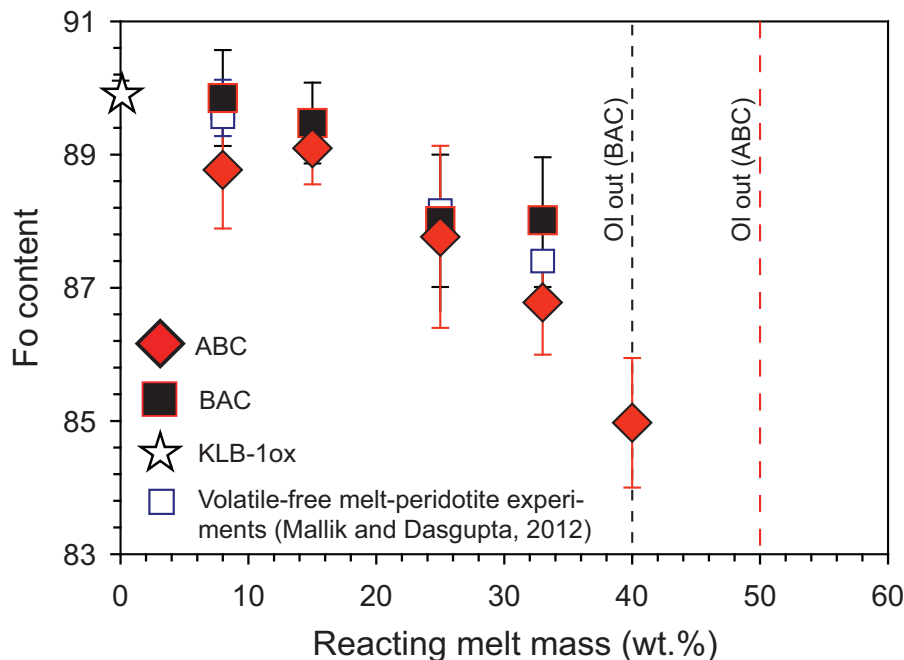
(continued)

Fig. 5. Forsterite content $\{[(molar\ MgO)/(molar\ MgO) + (molar\ FeO)] \times 100\}$ of olivine in the residue of melt–rock reaction plotted as a function of reacting eclogite melt mass (wt %). Also plotted for comparison are the residual olivine compositions from the CO_2-free equivalent of the BAC + peridotite experiments (Mallik & Dasgupta, 2012). The dashed lines are the same as in Fig. 4.

(2) The two-pyroxene thermometer of Brey & Kohler (1990) and garnet–clinopyroxene thermometer of Ravna (2000) were used to calculate the temperature of each experiment (T_{BKN} and T_{R00}; Table 2). The maximum deviations of the actual temperature of the experiment and calculated temperature for T_{BKN} is $53°C$ and for T_{R00} is $108°C$, both of which are within the uncertainty of the respective thermometers. This demonstrates that the experiments had approached equilibrium.

(3) $K_D^{Fe*-Mg}(ol-melt)$ (Table 4) varies from $0·31 \pm 0·03$ to $0·47 \pm 0·04$, which is consistent with the high $K_D^{Fe*-Mg}(ol-melt)$ values of $0·33–0·63$ obtained in previous studies on carbonated peridotite partial melting and magma–crustal carbonate interactions (Hirose, 1997; Dasgupta *et al.*, 2007; Mollo *et al.*, 2010). Moreover, the variation of $K_D^{Fe*-Mg}(ol-melt)$ as a function of the $FeO* + MgO$ of melts mimics the trend noted in previous studies (Kushiro & Walter, 1998; Filiberto & Dasgupta, 2011).

Phase compositions

Reacted melt

Reacted melt compositions (on a volatile-free basis) resulting from ABC + KLB-1 and BAC + KLB-1 mixtures are reported in Table 3 and plotted in Fig. 4 as a function of the initial mass of reacting melt. Reacted melt compositions from the volatile-free experiments of Mallik & Dasgupta (2012) are also plotted in the same figure for comparison.

For reacted melts in experiments with ABC, there is an overall decrease in SiO_2 from 30·1 to 27 wt %, MgO from 21·1 to 19·7 wt %, and Mg# from 73 to 69 for the increase of the original reacting melt mass from 15 to 50 wt %. An overall increase in Na_2O content from 4·1 to 6·7 wt % is also observed for the same range in melt–rock ratios as above. An initial decrease in TiO_2 from 6·3 to 2·8 wt %, FeO* from 14·2 to 10·8 wt %, CO_2 from 22·5 to 11·6 wt % from 15 to 25 wt % ABC-added runs is followed by an increase to 5·3 wt % for TiO_2, 15·6 wt % for FeO* and

Fig. 4. Continued

comparison, the glass compositions measured in 40 wt % and 50 wt % BAC-added runs and volatile-free melts produced at 1375°C, 3 GPa from basaltic-andesite–peridotite reaction experiments (Mallik & Dasgupta, 2012) are also plotted. The similarity between the compositions of averaged quench aggregates and glass in the 40 and 50% BAC-added experiments emphasizes the reliability of the reacted melt composition estimates in this study. It is observed that the mean of glass and quench aggregates are very close to each other (the range of difference between them being <1% to 10% relative for major elements). The short-dashed line represents the amount of BAC required to be flushed through peridotite to exhaust olivine from the residue. The long-dashed line represents the point of olivine exhaustion for flushing of ABC through peridotite. The $\pm 1\sigma$ error bars are based on replicate microprobe analyses.
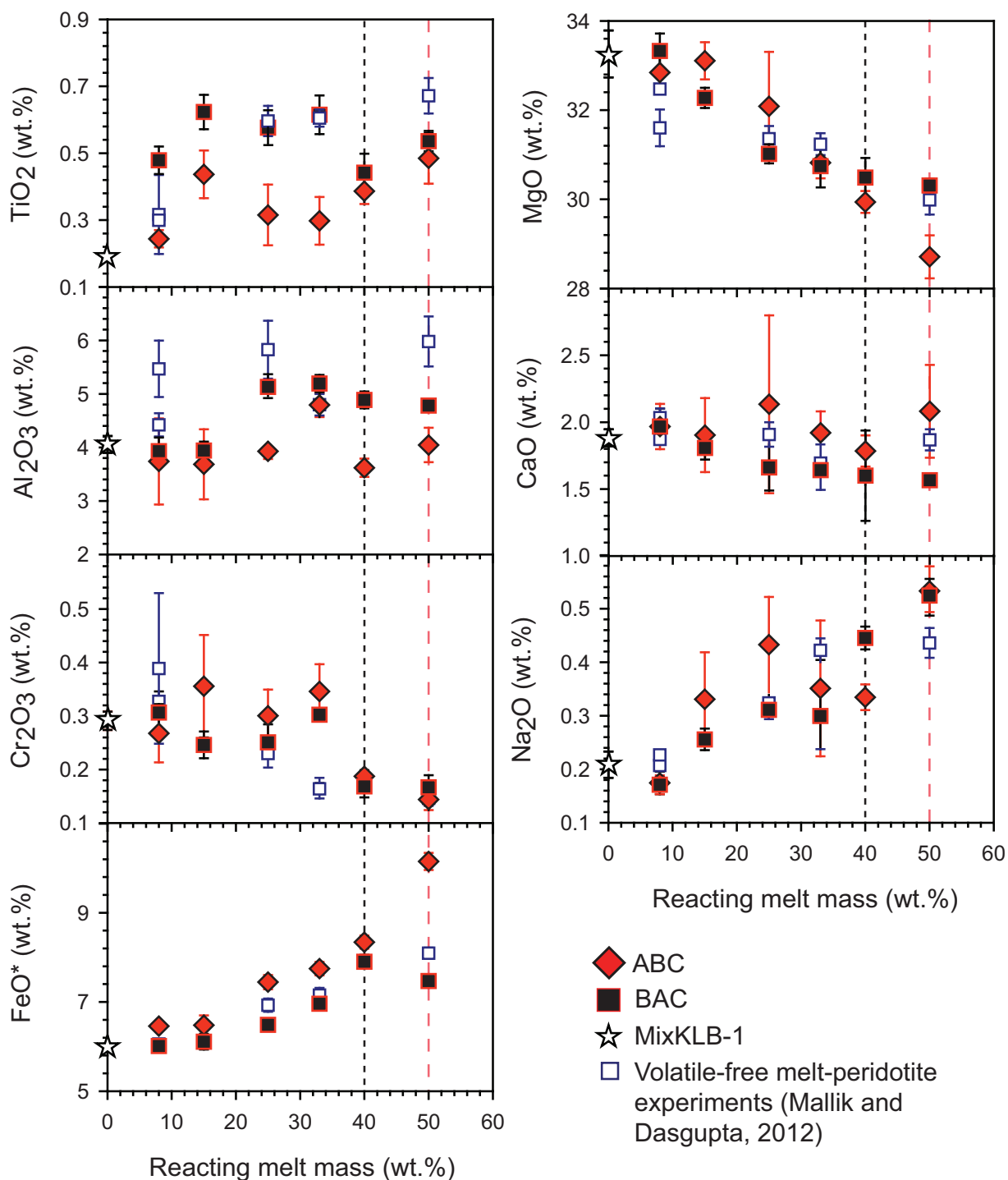
Fig. 6. Composition of orthopyroxenes from the residue of melt–rock reaction plotted as a function of reacting melt mass (wt %). Symbols, error bars and dashed lines are the same as in Fig. 4.

24·6 wt % for CO_2 up to 50 wt % ABC-added runs. An increase in Al_2O_3 content from 5·2 to 9·1 wt % and decrease in CaO content from 18 to 13 wt % is observed for reacting melt mass from 15 to 33 wt %, followed by a decrease to

4·1 wt % and increase to 21 wt % in Al_2O_3 and CaO respectively for reacting melt mass up to 50 wt %. In the case of BAC, with increasing added melt mass from 25 to 50 wt %, the reacted melt SiO_2 increases from 42·4 to
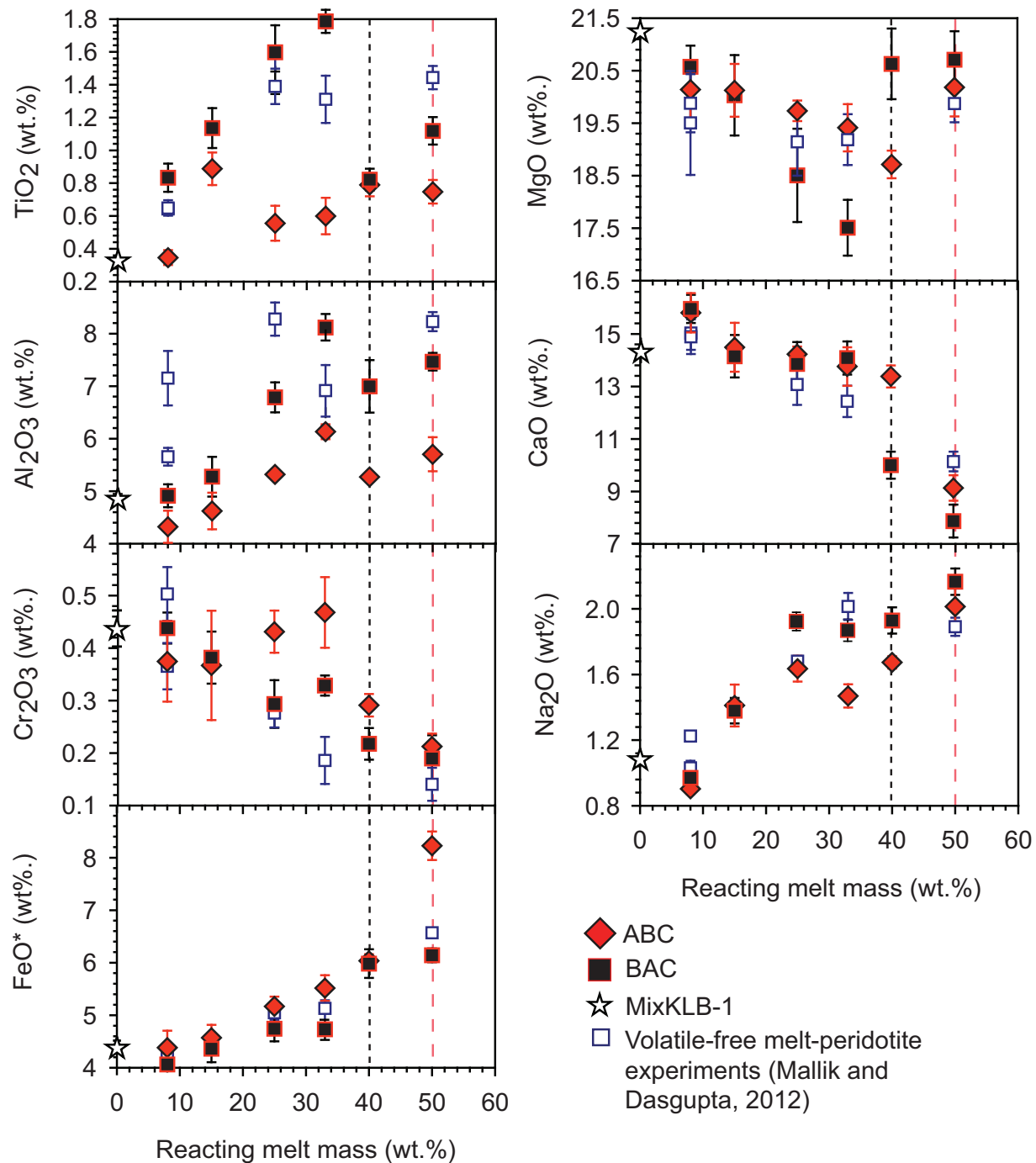
Fig. 7. Composition of clinopyroxenes from the residue of melt–rock reaction plotted as a function of reacting melt mass (wt %). Symbols, error bars and dashed lines are the same as in Fig. 4.

53·4 wt %, TiO_2 from 6·4 to 8·7 wt %, Al_2O_3 from 10·5 to 12·3 wt % , FeO from 10·3 to 6·5 wt %, MgO from 15·4 to 7·9 wt %, CaO from 10·3 to 7·3 wt %, Mg# from 73 to 68 and CO_2 from 12 to 6 wt %. Na_2O displays a slight decrease from 4 to 3·4 wt % with increasing melt mass from 25 to 50 wt %.

Olivine

Olivine compositions are reported in Table 4 and plotted as a function of increasing amount of melt added in Fig. 5.

Olivines from the carbonated melt–rock reaction experiments display a steady decrease in forsterite content from 90·1 to 85 for ABC and 88·6 for BAC for increasing
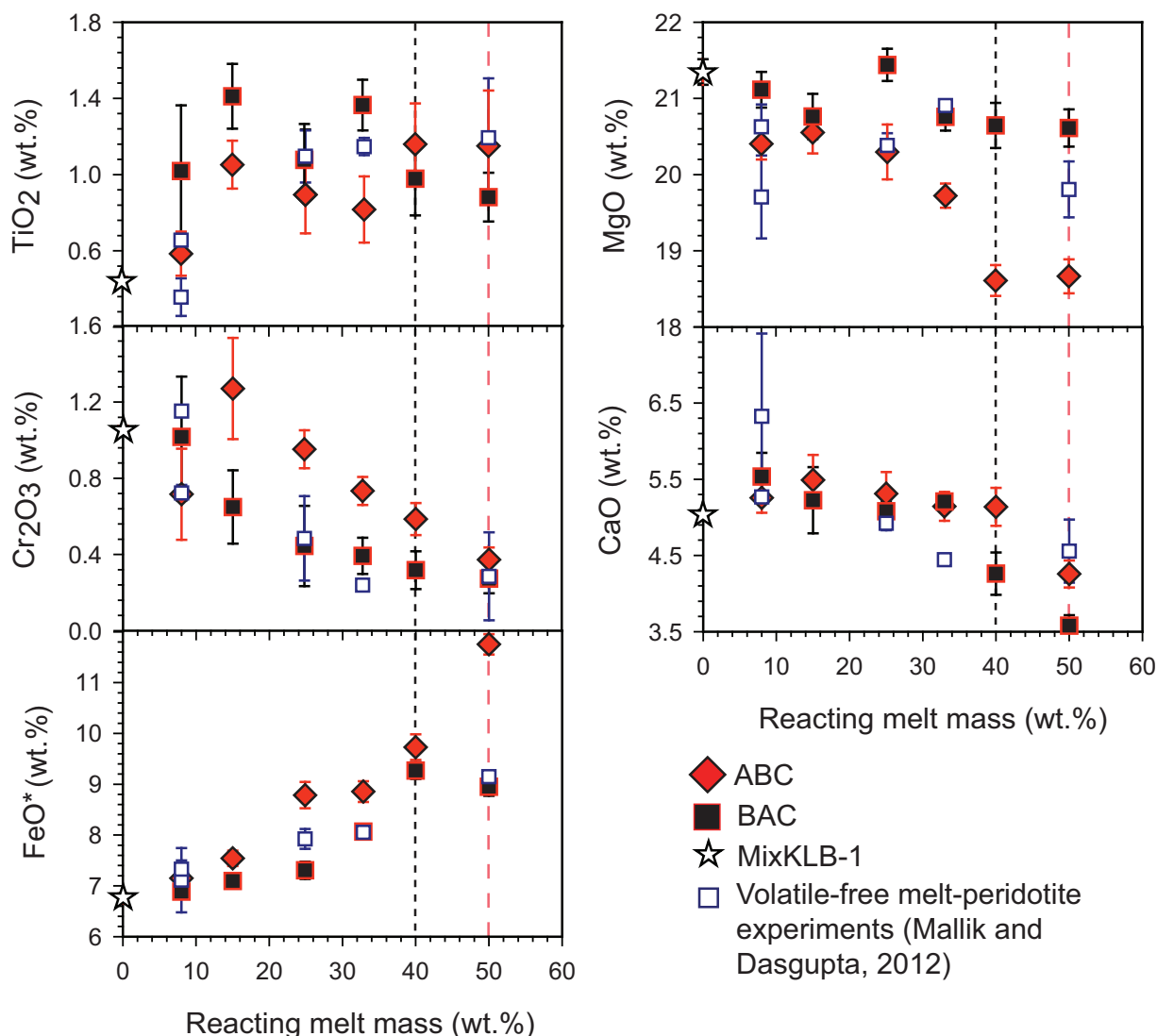
Fig. 8. Composition of garnets from the residue of melt–rock reaction plotted as a function of reacting melt mass (wt %). Symbols, error bars and dashed lines are the same as in Fig. 4.

amount of melt added from 0 to 40 wt % and 33 wt % respectively.

Orthopyroxene

Orthopyroxene compositions are reported in Table 5 and plotted as a function of increasing amount of melt added in Fig. 6.

Orthopyroxenes from the carbonated melt–rock reactions display an overall increase in concentrations of TiO_2 (from 0·19 to 0·48 wt % for ABC and 0·54 wt % for BAC), $FeO*$ (from 6 to 10 wt % for ABC and 7·5 wt % for BAC) and Na_2O (from 0·21 to 0·5 wt % for both ABC and BAC), and decrease in Cr_2O_3 (from 0·3 to 0·14 wt % for ABC and 0·17 wt % for BAC) and MgO (from 33 to 30 wt % for both ABC and BAC) with the reacting melt mass varying from 0 to 50 wt %. The trend displayed by

orthopyroxenes crystallized in experiments with BAC is similar to that displayed by orthopyroxenes from volatile-free melt–rock reaction experiments (Mallik & Dasgupta, 2012). Although there is no systematic trend in Al_2O_3 and CaO concentrations for orthopyroxenes from runs with ABC, a slight increase in Al_2O_3 from 4·06 to 4·78 wt % and decrease in CaO from 1·89 to 1·57 wt % is observed for BAC-added runs.

Clinopyroxene

Clinopyroxene compositions are reported in Table 6 and plotted as a function of increasing amount of added melt in Fig. 7.

Compositional trends for clinopyroxenes are similar to those of orthopyroxene for TiO_2, Cr_2O_3, FeO and Na_2O. There is no systematic variation in MgO with increase in

Table 4: Composition of olivines

Run no.:	G209	G217	G239	G240	G227	B126	B157	B222	B223
Starting melt:	ABC	ABC	ABC	ABC	ABC	BAC	BAC	BAC	BAC
Melt added (wt %):	8	15	25	33	40	8	15	25	33
n:	9	12	10	15	13	10	16	14	18
SiO_2	40·0(3)	40·4(4)	38·7(4)	39·8(3)	40·5(3)	40·4(2)	40·7(2)	40·4(8)	39·6(2)
TiO_2	b.d.l.	b.d.l.	b.d.l.	b.d.l.	b.d.l.	b.d.l.	b.d.l.	b.d.l.	b.d.l.
Al_2O_3	0·08(3)	0·08(2)	0·10(4)	0·1(1)	0·12(7)	0·2(2)	0·10(6)	0·2(5)	0·13(8)
Cr_2O_3	b.d.l.	b.d.l.	b.d.l.	b.d.l.	b.d.l.	b.d.l.	b.d.l.	b.d.l.	b.d.l.
FeO*	10·9(3)	10·7(2)	12·00(1)	12·7(1)	14·0(2)	10·0(2)	10·1(2)	11·3(6)	11·6(3)
MnO	0·09(2)	0·09(1)	0·103(7)	0·12(2)	0·11(1)	0·08(1)	0·07(1)	0·09(2)	0·09(2)
MgO	48·5(3)	49·2(2)	48·3(6)	46·6(3)	44·4(4)	49·6(3)	48·4(2)	48·1(5)	47·3(4)
CaO	0·170(8)	0·16(2)	0·17(3)	0·20(3)	0·3(3)	0·18(2)	0·17(1)	0·17(3)	0·20(7)
Na_2O	b.d.l.	b.d.l.	b.d.l.	b.d.l.	b.d.l.	b.d.l.	b.d.l.	b.d.l.	b.d.l.
K_2O	b.d.l.	b.d.l.	b.d.l.	b.d.l.	b.d.l.	b.d.l.	b.d.l.	b.d.l.	b.d.l.
Sum	99·81	100·81	99·47	99·58	99·37	100·60	99·57	100·37	98·94
Fo#	88·8(9)	89·1(5)	88(1)	86·8(8)	85·0(1)	89·8(7)	89·5(6)	88(1)	88(1)
$K_D^{Fe^*-Mg}$ (ol–melt)	—	0·33(4)	0·45(4)	0·36(3)	0·41(6)	—	—	0·35(5)	0·31(3)

*All Fe assumed to be FeO.
All oxide concentrations are reported in weight per cent. b.d.l., below detection limit. $K_D^{Fe^*-Mg}$ (ol–melt) is given by $(X_{Mg}^{Melt}/X_{Mg}^{Mineral})/(X_{Fe2+}^{Melt}/X_{Fe2+}^{Mineral})$.

Table 5: Composition of orthopyroxenes

Run no.:	G209	G217	G239	G240	G227	G229	B126	B157	B222	B223	G231	G226
Starting melt:	ABC	ABC	ABC	ABC	ABC	ABC	BAC	BAC	BAC	BAC	BAC	BAC
Melt added (wt %):	8	15	25	33	40	50	8	15	25	33	40	50
n:	12	26	9	9	8	16	27	12	42	45	23	11
SiO_2	53·8(5)	54·1(5)	52·8(7)	53·3(3)	54·3(4)	53·3(4)	53·8(8)	54·1(2)	54·4(7)	53·7(1)	54·3(8)	53·5(2)
TiO_2	0·24(3)	0·44(7)	0·32(9)	0·30(7)	0·39(4)	0·48(8)	0·48(4)	0·62(5)	0·57(6)	0·63(6)	0·44(6)	0·54(3)
Al_2O_3	3·7(8)	3·7(7)	3·9(1)	4·8(2)	3·6(2)	4·0(3)	3·9(3)	3·9(2)	5·1(3)	5·2(5)	4·9(2)	4·78(1)
Cr_2O_3	0·27(5)	0·36(1)	0·30(5)	0·35(5)	0·19(1)	0·14(2)	0·31(4)	0·25(3)	0·25(5)	0·30(3)	0·17(2)	0·17(2)
FeO*	6·46(1)	6·5(2)	7·4(2)	7·7(2)	8·3(1)	10·2(2)	6·0(1)	6·1(2)	6·5(2)	7·0(2)	7·9(2)	7·5(1)
MnO	0·08(3)	0·09(3)	0·09(5)	0·12(2)	0·13(4)	0·13(3)	0·08(3)	0·08(3)	0·07(2)	0·09(2)	0·05(2)	0·07(3)
MgO	32·8(4)	33·1(4)	32(1)	30·8(3)	29·9(2)	28·7(5)	33·3(4)	32·3(2)	31·0(4)	30·7(6)	30·5(4)	30·3(2)
CaO	2·0(1)	1·9(3)	2·1(7)	1·9(2)	1·8(1)	2·1(3)	2·0(2)	1·81(9)	1·7(1)	1·64(1)	1·6(3)	1·57(3)
Na_2O	0·17(2)	0·33(9)	0·43(9)	0·4(1)	0·33(2)	0·53(5)	0·17(2)	0·26(2)	0·31(2)	0·30(3)	0·45(2)	0·52(3)
K_2O	b.d.l	b.d.l	b.d.l	b.d.l	b.d.l	b.d.l	b.d.l	b.d.l	b.d.l	b.d.l	b.d.l	b.d.l
Sum	99·61	100·46	99·55	99·73	99·03	99·55	100·10	99·41	99·87	99·59	100·29	98·96
$K_D^{Fe^*-Mg}$ (opx–melt)	—	0·31(4)	0·42(4)	0·34(4)	0·36(5)	0·45(4)	—	—	0·32(1)	0·28(3)	0·28(2)	0·30(2)

All oxide concentrations are reported in weight per cent. b.d.l., below detection limit. $K_D^{Fe^*-Mg}$ (opx–melt) is given by $(X_{Mg}^{Melt}/X_{Mg}^{Mineral})/(X_{Fe2+}^{Melt}/X_{Fe2+}^{Mineral})$.
*All Fe assumed to be FeO.

reacting melt mass, whereas a distinct increase in Al_2O_3 (from 4·9 to 5·7 wt % for ABC and to 7·5 wt % for BAC) and decrease in CaO concentrations (from 14·4 to 9·1 wt % for ABC and to 7·9 wt % for BAC) is observed for added melt masses varying from 0 to 50 wt %.

Garnet

Garnet compositions are reported in Table 7 and plotted as a function of increasing amount of melt added in Fig. 8.

Garnet compositions from carbonated melt–rock reaction experiments display a steady increase in FeO* (from

Table 6: Composition of clinopyroxenes

Run no.:	G209	G217	G239	G240	G227	G229	B126	B157	B222	B223	G231	G226
Starting melt:	ABC	ABC	ABC	ABC	ABC	ABC	BAC	BAC	BAC	BAC	BAC	BAC
Melt added (wt %):	8	15	25	33	40	50	8	15	25	33	40	50
n:	10	13	8	23	8	19	30	12	18	13	15	21
SiO_2	53·6(5)	53·4(4)	52·8(3)	52·1(4)	53·0(2)	54·0(2)	52·5(6)	53·0(5)	51·3(4)	49·0(4)	54·3(4)	53·8(2)
TiO_2	0·35(4)	0·89(1)	0·6(1)	0·6(1)	0·79(7)	0·75(7)	0·83(9)	1·1(1)	1·6(2)	1·78(7)	0·82(7)	1·12(8)
Al_2O_3	4·3(3)	4·6(3)	5·32(9)	6·1(1)	5·27(5)	5·7(3)	4·9(2)	5·3(4)	6·8(3)	8·2(2)	7·0(5)	7·5(2)
Cr_2O_3	0·37(8)	0·4(1)	0·43(4)	0·47(7)	0·29(2)	0·21(2)	0·44(3)	0·38(5)	0·29(5)	0·33(2)	0·22(3)	0·19(4)
FeO^*	4·4(3)	4·6(2)	5·2(2)	5·5(2)	6·0(1)	8·2(3)	4·1(1)	4·4(3)	4·7(2)	4·8(2)	6·0(3)	6·1(1)
MnO	0·09(3)	0·08(2)	0·10(3)	0·10(3)	0·10(2)	0·14(3)	0·07(2)	0·07(2)	0·08(2)	0·08(2)	0·06(3)	0·08(3)
MgO	20·1(5)	20·1(5)	19·7(2)	19·4(4)	18·7(3)	20·2(6)	20·6(4)	20·0(8)	18·5(9)	17·5(5)	20·6(7)	20·7(5)
CaO	15·8(7)	14·5(9)	14·2(3)	13·8(7)	13·4(4)	9·1(5)	16·0(5)	14·1(8)	13·9(8)	14·1(6)	10·0(5)	7·9(6)
Na_2O	0·90(3)	1·4(1)	1·64(8)	1·47(7)	1·67(4)	2·0(1)	0·97(6)	1·38(8)	1·92(6)	1·87(7)	1·93(8)	2·178)
K_2O	b.d.l	b.d.l	b.d.l	b.d.l	b.d.l	b.d.l	b.d.l	b.d.l	b.d.l	b.d.l	b.d.l	b.d.l
Sum	99·93	99·98	100·00	99·60	99·29	100·32	100·34	99·83	99·06	97·52	100·90	99·55

All oxide concentrations are reported in weight per cent. b.d.l., below detection limit.
*All Fe assumed to be FeO.

Table 7: Composition of garnets

Run no.:	G209	G217	G239	G240	G227	G229	B126	B157	B222	B223	G231	G226
Starting melt:	ABC	ABC	ABC	ABC	ABC	ABC	BAC	BAC	BAC	BAC	BAC	BAC
Melt added (wt %):	8	15	25	33	40	50	8	15	25	33	40	50
n:	9	14	14	14	12	20	15	9	13	10	13	14
SiO_2	41·7(2)	41·4(3)	41·2(6)	41·3(4)	41·6(3)	40·9(4)	41·2(5)	41·5(2)	41·4(5)	40·1(4)	41·9(1)	41·3(2)
TiO_2	0·6(1)	1·1(1)	0·9(2)	0·8(2)	1·2(2)	1·2(3)	1·0(3)	1·4(2)	1·1(2)	1·4(1)	1·0(2)	0·9(1)
Al_2O_3	23·6(6)	22·6(3)	22·8(4)	23·2(3)	22·9(3)	23·1(5)	23·3(6)	23·0(6)	23·0(8)	22·5(3)	23·5(6)	23·6(2)
Cr_2O_3	0·7(2)	1·3(3)	0·95(1)	0·73(7)	0·59(8)	0·37(6)	1·0(3)	0·6(2)	0·4(2)	0·39(1)	0·32(1)	0·27(8)
FeO^*	7·1(2)	7·5(2)	8·7(3)	8·8(2)	9·7(3)	11·8(2)	6·9(1)	7·1(1)	7·3(2)	8·0(1)	9·3(2)	9·0(2)
MnO	0·17(1)	0·19(1)	0·20(1)	0·22(1)	0·22(1)	0·242(1)	0·15(1)	0·14(1)	0·15(1)	0·17(1)	0·11(2)	0·14(1)
MgO	20·4(2)	20·6(3)	20·3(4)	19·7(2)	18·6(2)	18·7(2)	21·1(2)	20·8(3)	21·4(2)	20·8(2)	20·6(3)	20·6(2)
CaO	5·3(2)	5·5(3)	5·3(3)	5·1(2)	5·1(2)	4·3(2)	5·5(3)	5·2(4)	5·1(1)	5·2(1)	4·3(3)	3·6(1)
Na_2O	b.d.l	b.d.l	b.d.l	b.d.l	b.d.l	b.d.l	b.d.l	b.d.l	b.d.l	b.d.l	b.d.l	b.d.l
K_2O	b.d.l	b.d.l	b.d.l	b.d.l	b.d.l	b.d.l	b.d.l	b.d.l	b.d.l	b.d.l	b.d.l	b.d.l
Sum	99·61	100·07	100·41	99·98	100·01	100·41	100·23	99·77	99·92	98·66	100·94	99·32

All oxide concentrations are reported in weight per cent. b.d.l., below detection limit.
*All Fe assumed to be FeO.

6·7 to 11·8 wt % for ABC and 9 wt % for BAC) and decrease in Cr_2O_3 (from 1·05 to 0·37 wt % for ABC and 0·27 wt % for BAC) when the proportion of initial reacting melt mass varied from 0 to 50 wt %; these trends are similar to those for garnets in the volatile-free melt–rock reaction experiments reported by Mallik & Dasgupta (2012). In the case of TiO_2, there is an overall increase from 0·44 to 1·15 wt % for ABC-added runs from no-melt-added to the 50 wt % melt-added run. Garnets from runs with BAC display an overall increase in TiO_2 concentrations from

0·44 to 0·88 wt % from no-melt-added to 50 wt % melt-added run. The ABC-added experiments also display a steady decrease in MgO concentration from 21·3 to 18·7 wt % for initial, reacting melt mass varying from 0 to 50 wt %. The MgO concentrations of garnets decrease slightly from 21·3 to 20·6 wt % with increasing melt added for experiments performed with BAC.

DISCUSSION
Phase relations of melt–rock reactions between eclogite-derived carbonated silicate melt and peridotite

Using phase proportions, calculated by mass balance (Table 2; Fig. 3), for both the melt–rock mixtures and the melt-free, subsolidus peridotite at the same conditions, chemical reactions for each experiment have been obtained (Table 8). In all the experiments, orthopyroxene and garnet are produced at the expense of olivine and carbonated silicate melt. These reactions are corroborated by (1) decrease in olivine modal proportion ultimately leading to exhaustion at high melt–rock ratios and (2) increase in modal proportions of orthopyroxene and garnet for both series of melt–rock reaction experiments. With increasing melt–rock ratios, the peridotite is transformed to webster-ite (at 50 wt % melt added for ABC and 40 wt % melt added for BAC).

Clinopyroxene is overall produced, except for four experiments: 15 and 25 wt % ABC-added and 8 and 25 wt % BAC-added runs. In general, clinopyroxene production per gram of melt is lower than garnet and orthopyroxene production.

Evolution of carbonated alkali basalt (ABC) owing to reaction with garnet peridotite

The melts from ABC–KLB-1 mixtures display an evolution in composition with changing melt–rock ratios and the trends for each oxide component are discussed below.

SiO_2

The SiO_2 concentration of the reacted melts is lower than that of the starting melt ABC owing to consumption of SiO_2 from the melt to crystallize orthopyroxene at the expense of olivine following reaction (1). It is observed to increase initially in the 15–25 wt % ABC-added runs, followed by a decrease in the 33–50 wt % runs (Fig. 4). This trend is mirrored by the change in CO_2 concentration in the reacted melts as a function of melt-mass added. Except for the 50 wt % ABC-added run, the ABC-derived reacted melts have their activity of SiO_2 buffered by coexisting olivine and orthopyroxene. Dissolution of CO_2 as CO_3^{2-} enhances the activity coefficient of SiO_2 in reacted melts, thereby decreasing the concentration of SiO_2 (as the activity of SiO_2 is buffered and changes little).

Thus, a higher CO_2 concentration in the reacted melt results in a lower SiO_2 concentration and vice versa.

TiO_2

The TiO_2 concentration of the reacted melts is affected by (1) the bulk Ti content of the melt–rock mixture, (2) the final melt fraction, and (3) the bulk partitioning of Ti between the residue and the melt, (D_{Ti}), which in turn is affected by the modal mineralogy of the residual assemblage. TiO_2 in the reacted melt is higher than that in ABC owing to melt consumption and the incompatible behavior of the oxide during reactive crystallization of carbonated alkalic basalt in an olivine-bearing peridotitic matrix. A decrease in TiO_2 concentration from 15 to 25 wt % ABC-added runs is observed owing to an increase in the clinopyroxene modal proportion, causing D_{Ti} to increase. However, this decrease in TiO_2 content is followed by a steady increase up to the 50 wt % ABC-added run because of the increasing TiO_2 content in the bulk melt–rock mixture overriding any effect of increasing garnet modal proportions (and as a result D_{Ti}) (Fig. 3).

Al_2O_3

The reacted melts have lower Al_2O_3 than ABC owing to the crystallization of Al-bearing orthopyroxene, clinopyroxene and garnet. The initial trend of increasing Al_2O_3 concentration with increasing reacting melt mass from 15 to 33 wt % is due to increasing bulk alumina content at similar residual garnet mode; the drop in Al_2O_3 in the 40 and 50 wt % melt-added experiments (Fig. 4) is the result of greater amounts of residual garnet. The similarity in the evolution trend of Al_2O_3 to that of SiO_2 is also suggestive of the effect of dilution of the Al_2O_3 content of the reacted melt by CO_2.

$FeO*$

Reacted melts derived from ABC tend overall to become enriched in FeO* at higher melt–rock ratios owing to increasing Fe in the bulk composition.

MgO

The MgO content in the reacted melts is higher than in the starting melt ABC owing to interaction with the peridotite (Mg-rich lithology), and decreases slightly with increasing melt–rock ratio owing to the greater buffering capacity of the melt as compared with peridotite.

CaO

Whereas the CaO contents in pyroxenes and garnet decrease with increasing melt–rock ratio (Figs 6–8), the modal proportions of orthopyroxene and garnet increase (clinopyroxene mode does not vary significantly with melt–rock ratio), with the net effect of bulk D_{Ca} remaining constant. However, within error, an overall increase in Ca concentration is observed with increasing melt–rock ratio

Table 8: Chemical reactions for the experiments

Starting materials used	Run no.	Melt added (wt %)	Chemical reactions (per gram of melt)
ABC + KLB-1ox	G209	8	0·9 ol + 1·0 melt = 0·6 opx + 0·2 cpx + 1·1 gt
ABC + KLB-1ox	G217	15	1·7 ol + 0·5 cpx + 1·0 melt = 2·4 opx + 0·8 gt
ABC + KLB-1ox	G239	25	1·6 ol + 0·1 cpx + 1·0 melt = 2·0 opx + 0·7 gt
ABC + KLB-1ox	G240	33	1·0 ol + 1·0 melt = 1·2 opx + 0·2 cpx + 0·6 gt
ABC + KLB-1ox	G227	40	0·7 ol + 1·0 melt = 0·9 opx + 0·1 cpx + 0·7 gt
ABC + KLB-1ox	G229	50	1·0 ol + 1·0 melt = 1·2 opx + 0·2 cpx + 0·6 gt
BAC + KLB-1ox	B126	8	2·7 ol + 0·6 cpx + 1·0 melt = 3·7 opx + 0·6 gt
BAC + KLB-1ox	B157	15	1·8 ol + 1·0 melt = 1·8 opx + 0·2 cpx + 0·8 gt
BAC + KLB-1ox	B222	25	3·2 ol + 0·8 cpx + 1·0 melt = 4·9 opx + 0·1 gt
BAC + KLB-1ox	B223	33	1·5 ol + 1·0 melt = 2·2 opx + 0·003 cpx + 0·3 gt
BAC + KLB-1ox	G231	40	1·2 ol + 1·0 melt = 1·5 opx + 0·3 cpx + 0·4 gt
BAC + KLB-1ox	G226	50	1·1 ol + 1·0 melt = 1·0 opx + 0·7 cpx + 0·4 gt

All the reactions have been normalized to 1 g of melt. The reactions have been balanced only for major element components SiO_2, TiO_2, Al_2O_3, FeO*, MgO, CaO and Na_2O. CO_2 as well as minor elements such as Cr_2O_3, MnO and K_2O were ignored for mass balance.

owing to enrichment of Ca in the bulk melt–rock mixture and to enhancement of CO_2 in the reacted melt with increasing melt–rock ratio. The trend of increasing CaO with increasing CO_2 of the melt is broadly consistent with the melt compositional trend observed in carbonated peridotite partial melting experiments (Dasgupta *et al.*, 2007).

Na_2O
Enrichment in the Na_2O content of the melt is observed with increasing melt–rock ratio owing to the increasing Na_2O concentration of the bulk composition of the melt–rock mixture.

$Mg\#$
The decreasing trend of $Mg\#$ with increasing melt–rock ratio is a function of the decreasing $Mg\#$ of the bulk melt–rock mixture as the melt–rock ratio increases.

CO_2
CO_2 concentration in the reacted melts depends on two factors, (1) bulk CO_2 concentration and (2) modal proportion of melt after melt–rock reaction. At a constant melt mass, a higher bulk CO_2 concentration will yield a melt with higher CO_2, whereas at a constant bulk CO_2 concentration a higher modal proportion of reacted melt reduces the CO_2 concentration owing to the near-perfect incompatibility of CO_2. An initial decrease in CO_2 concentration of the reacted melt is observed in the 15–33 wt % ABC-added runs owing to an increase in melt modal proportion. This is followed by a near-steady increase in CO_2 content until 50 wt % melt is added, because of an interplay of the melt modal proportion changing only modestly and

the bulk CO_2 concentration of the melt–rock mixture increasing with the higher amount of melt added.
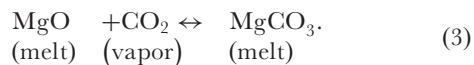
Evolution of carbonated basaltic andesite (BAC) owing to reaction with garnet peridotite: an assessment of the effect of CO_2 on phase equilibria during reactive infiltration of eclogite partial melt into peridotite

Comparison of reacted melt compositions saturated in olivine + orthopyroxene + clinopyroxene + garnet, derived from the BAC + KLB-1 mixture (specifically 25% BAC-added mixture), with the volatile-free experiments of Mallik & Dasgupta (2012) suggests that the former are lower in SiO_2 and Al_2O_3, and higher in MgO and CaO in saturation with a four-phase assemblage. The notable exception is FeO*, for which the melts derived from partial reactive crystallization of BAC at intermediate melt–rock ratios are similar to or slightly lower in FeO* compared with the reacted melts from volatile-free melt–rock reaction, suggesting no strong influence of dissolved CO_2 in stabilizing melt of a different FeO* content. The Na_2O contents of the melts evolved from BAC are slightly lower than the volatile-free, reacted melts and these differences, once again, probably result from a slight difference in the Na_2O content of the carbonated- and volatile-free starting melts BAC and G2PM1, respectively. It is plausible that an increase in $Mg\#$ (maximum relative difference being $\sim7\%$) of the intermediate melt–rock ratio BAC-derived melts with respect to reacted melts from volatile-free melt–rock mixtures is due to the dissolved CO_2 in the BAC-derived reacted melts enhancing the MgO content

of partial melts by forming $MgCO_3$ complexes (e.g. Guillot & Sator, 2011), and hence that a carbonated melt in equilibrium with all four lherzolitic phases is richer in MgO than its carbonate-free counterpart.

CO_2 concentrations in carbonated silicate melts display a negative correlation with SiO_2 concentrations and a positive correlation with CaO concentrations similar to observations by Dasgupta et al. (2007, 2013). Diminishing SiO_2 concentrations with increasing CO_2 concentrations in olivine- and opx-saturated melts have been attributed to the effect of an increased activity coefficient of SiO_2 by dissolved CO_2 in the form of carbonate complexes. On the other hand, an increasing CaO concentration in melts with higher CO_2 has been explained as the effect of a decreasing activity coefficient of CaO in the melt as CaO reacts with CO_2 to form $CaCO_3$ complexes in the melt. Lower Al_2O_3 in the carbonated melt–rock reaction experiments as compared with the volatile-free runs is due to the increased stability of garnet and aluminous orthopyroxene in the residue (Fig. 3).

Similar to CaO (Dasgupta et al., 2007), MgO can complex with CO_2 in silicate melts to produce carbonate complexes:

$$\begin{array}{ccc} MgO & +CO_2 \leftrightarrow & MgCO_3. \\ (melt) & (vapor) & (melt) \end{array} \tag{3}$$

A recent study by Guillot & Sator (2011) confirmed that the propensity of network-modifying cations such as Ca^{2+}, Fe^{2+} and Mg^{2+} to bond with carbonates (whether the carbonates are associated with bridging or non-bridging oxygens) is much higher than that of network-forming cations such as Si^{4+}, Ti^{4+} and Al^{3+}, irrespective of the degree of silica-saturation of the melt concerned. Although our study does not conclusively suggest any effect of CO_2 on the FeO* content of the reacted melt, a reduction in the activity coefficient of MgO (along with CaO) can be suggested based on the tendency of MgO (and CaO) to be enriched in carbonated silicate melts.

Enrichment of TiO_2 in reacted carbonated silicate melt in the MORB-eclogite–peridotite system

The TiO_2 enrichment of silica-poor, alkalic basalts in general and those from ocean islands in particular is of considerable interest (Dasgupta et al., 2006, 2007; Prytulak & Elliott, 2007). The reacted melts from this study are rich in TiO_2, therefore it is worth constraining what variables truly affect the TiO_2 content of magma derived from a hybrid mantle. Higher TiO_2 in our CO_2-bearing reacted melts is due in part to greater melt consumption in this study as compared with the volatile-free experiments of Mallik & Dasgupta (2012) (Fig. 3); that is, for a given melt–rock ratio, greater orthopyroxene precipitation and as a consequence melt consumption leads to enrichment of incompatible elements in the remaining melt. Therefore, one

indirect effect of the presence of dissolved carbonates in the melt is to cause TiO_2 enrichment through expansion of the orthopyroxene stability field. Although the difference between the TiO_2 contents of reacted melts derived from BAC and those from the CO_2-free experiments of Mallik & Dasgupta (2012) can in part be explained by the difference in the resulting melt fractions, the role of melt silica content is also important. It has long been known that the diminished concentration of SiO_2 in a melt saturated with olivine + orthopyroxene (i.e. at a buffered silica activity) causes enrichment of TiO_2 (Delano, 1980; Wagner & Grove, 1997; Xirouchakis et al., 2001). Hence one might expect that partial melts with lower silica contents should have higher TiO_2 contents. Figure 9 shows that this indeed is the case for reacted melts derived both from BAC and from ABC. Therefore, another role of dissolved carbonate is indirectly to enhance the TiO_2 content in reacted melts by reducing the melt silica content. However, melts derived from BAC are much more enriched in TiO_2 at given silica content than those derived from ABC (Fig. 9). This is due in part to the difference in the TiO_2 content of the starting eclogite melt BAC (5·66 wt %) and ABC (2·87 wt %); that is, different bulk TiO_2 content of BAC + KLB-1 and ABC + KLB-1 mixtures at a given melt:rock ratio. Perhaps more importantly, however, the data indicate that highly carbonated melts are not characterized by TiO_2 enrichment with diminishing silica following the same trend as CO_2-free or CO_2-poor melts. This is probably due to the fact that TiO_2 forms oxide complexes in the melt by bonding with FeO and MgO and in strongly carbonated melts the available nonbridging oxygens are reduced by the formation of $MgCO_3$ and $FeCO_3$ complexes. Indeed, it can be observed that all the strongly carbonated experimental melts that are olivine + orthopyroxene saturated (ABC-derived melts, this study; Hirose, 1997; Dasgupta et al, 2007, 2013) define a steep negative trend in melt SiO_2–TiO_2 compositional space that is distinct from that for melts that are non-carbonated or relatively CO_2-poor, such as the BAC-derived melts (Fig. 9).

Expansion of orthopyroxene and garnet stability at the liquidus owing to dissolved CO_2

In our study, we observed an increase in orthopyroxene and garnet modal proportions in the residue of melt–rock reaction for BAC with respect to similar experiments with the CO_2-free equivalent of BAC (G2PM1; Mallik & Dasgupta, 2012). Also, olivine is exhausted for a reacting BAC mass between 33 and 40 wt %, whereas in the G2PM1–KLB-1 reactions (Mallik & Dasgupta, 2012) it is exhausted between a reacting melt mass of 40 and 50 wt %, which indicates more efficient destabilization of olivine at the basalt liquidus in the presence of CO_2. Furthermore, the modal abundances of residual clinopyroxene at a given melt:rock ratio in our study are somewhat
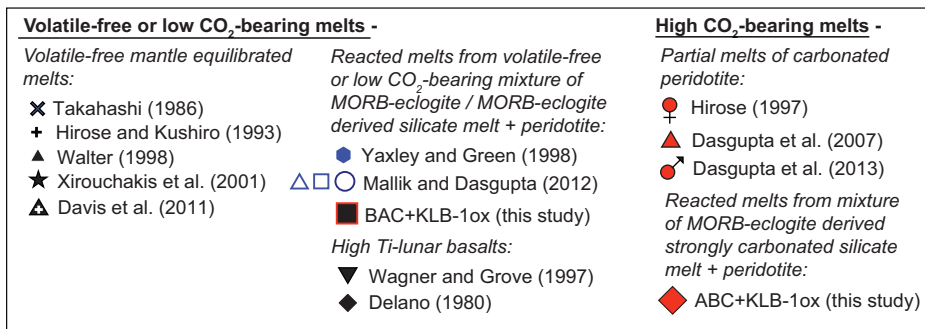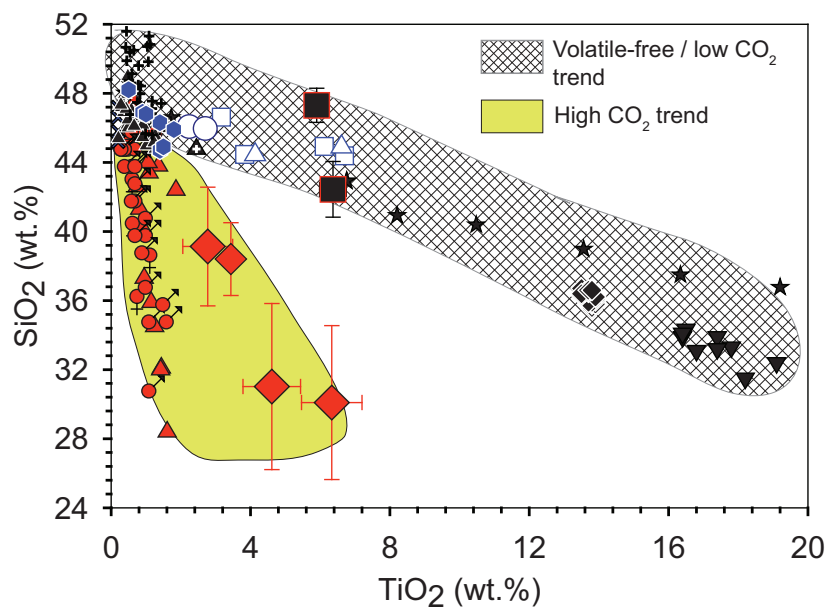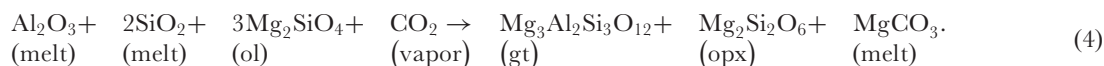
Fig. 9. SiO_2 (wt %) vs TiO_2 (wt %) in experimental melts saturated with olivine and orthopyroxene. The TiO_2 concentration of the melts increases linearly with decreasing SiO_2, with the degree of TiO_2 enrichment for a given SiO_2 concentration being lower for strongly carbonated melts (see text for further details) as compared with volatile-free or low CO_2-bearing melts. Volatile-free mantle equilibrated melts (Takahashi, 1986; Hirose & Kushiro, 1993; Walter, 1998; Xirouchakis et al., 2001; Davis et al., 2011), reacted melts from volatile-free or low-CO_2 mixture of MORB-eclogite or MORB-eclogite-derived silicate melt + peridotite (Yaxley & Green, 1998; Mallik & Dasgupta, 2012; BAC + KLB-1ox from this study) and high Ti-lunar basalts (Delano, 1980; Wagner & Grove, 1997) define the high-TiO_2 trend at a given SiO_2 content. Partial melts of carbonated peridotite (Hirose, 1997; Dasgupta et al., 2007, 2013) and reacted melts from mixtures of strongly carbonated MORB-eclogite-derived melt + peridotite (ABC + KLB-1ox from this study) describe the low-TiO_2 trend at a given SiO_2 content.

lower than those observed in CO_2-free melt–peridotite reaction experiments (Fig. 3; Mallik & Dasgupta, 2012). Enhanced consumption of Ca-rich pyroxene in the present study of BAC + KLB-1 reactions can be explained by complexation of Ca^{2+} and CO_3^{2-} in the reacted melt, which must lower the partition coefficient of Ca between cpx and melt compared with its value in CO_2-free melt-bearing systems.

Previous studies have suggested the expansion of orthopyroxene and garnet stability at the expense of olivine and clinopyroxene at the high-pressure liquidus of basalt in the presence of CO_2 (e.g. Brey & Green, 1975, 1977; Kushiro, 1975; Dasgupta et al., 2007). Dissolution of CO_2 in silicate melts by complexing with MgO and CaO reduces the activity of these network-modifying oxides and simultaneously enhances the activity coefficients of SiO_2 and Al_2O_3 in the melt by creating bridging oxygens. This explains why CO_2 dissolution in silicate melts promotes the stability of garnet and orthopyroxene at the liquidus. The process can be illustrated by the following reaction:

$$\underset{\text{(melt)}}{Al_2O_3} + \underset{\text{(melt)}}{2SiO_2} + \underset{\text{(ol)}}{3Mg_2SiO_4} + \underset{\text{(vapor)}}{CO_2} \rightarrow \underset{\text{(gt)}}{Mg_3Al_2Si_3O_{12}} + \underset{\text{(opx)}}{Mg_2Si_2O_6} + \underset{\text{(melt)}}{MgCO_3}. \tag{4}$$

Comparison of melting reactions constrained in previous peridotite partial melting experiments with CO_2 (e.g. Dasgupta *et al.*, 2007) or without CO_2 (e.g. Walter, 1998) suggests that dissolved carbonate in the melt probably expands the garnet stability field and as a consequence lowers the alumina content of carbonated partial melts. However, because carbonated silicate melting of natural peridotite takes place at distinctly lower temperatures than the volatile-free peridotite solidus (Wendlandt & Mysen, 1980; Hirose, 1997; Dasgupta *et al.*, 2007, 2013), it is unclear whether the increased stability of garnet in carbonated systems is due to the difference in melt composition or to a lower temperature of melting. Comparison of our present study (experiments on BAC + KLB-1 mixtures) with that of Mallik & Dasgupta (2012) confirms that the presence of dissolved carbonates in the melt definitely enhances garnet stability, even at constant temperature.

Transition from basanite to melilitite and silica-rich basaltic andesite to nephelinitic basanite

Figure 10 shows the classification of alkali basalts according to their degree of silica-undersaturation, following the classification scheme of Le Bas (1989), where the melts become increasingly silica-poor from basanite to nephelinite and finally to melilitite. ABC is an alkalic basalt (basanite) to start with and the reacted melts derived from ABC, irrespective of melt–rock ratio, evolve to melilitite upon reaction with peridotite in the presence of CO_2. BAC, on the other hand, is a silica-rich basaltic andesite and the reacted melts at intermediate melt–rock ratios (25 wt % and 33 wt % melt added) (i.e. in the presence of olivine + orthopyroxene + clinopyroxene + garnet) evolve to silica-poor basanites or nephelinitic basanites upon reaction with peridotite under the influence of CO_2. The effect of CO_2 is obvious in this case when the reacted melts, at intermediate melt–rock ratios, are compared with reacted melts under volatile-free conditions (Mallik & Dasgupta, 2012). Whereas the reacted melts derived from G2PM1 [CO_2-free starting melt composition in the study of Mallik & Dasgupta (2012)] evolve only up to basanite in terms of their degree of silica-undersaturation, even at the lowest melt–rock ratio of 8 wt % melt added, the CO_2-bearing basaltic andesite BAC evolves to a silica-poor basanite or nephelinitic basanite at an intermediate (25%) melt–rock ratio. This profound effect of lowering the silica concentration in the melt with just 2·6 wt % of dissolved CO_2 in a siliceous melt and no more than 0·86 wt % in the bulk melt–rock mixture is interesting because this process obviates the requirement for generating a silica-under-saturated melt from partial melting of Si-deficient eclogite or pyroxenite to explain the genesis of alkali basalts. In fact, our study demonstrates how a minute amount of

CO_2 (the CO_2 may be derived from carbonatites, a CO_2-rich fluid or by reaction of carbon-free siliceous partial melt with carbon present in the background mantle) dissolved in a MORB-eclogite-derived siliceous melt can cause a transition from silica-saturated to silica-under-saturated compositions upon reactive infiltration into peridotite. In fact, given the trend of melt composition with melt:rock ratio (Figs 4 and 10), reactive infiltration of lower melt masses than those that are being explored here would probably result in nephelinite or even melilititic reacted melt compositions. The higher melt–rock ratio experiments for BAC (40 and 50 wt % melt added) are less silicic than BAC itself, but not as silica-poor as the intermediate melt–rock ratio melts, and this can be attributed to the higher buffering capacity of the siliceous melts in these experiments and the exhaustion of orthopyroxene.

An interesting aspect worthy of further attention is that the vectors denoting the evolution of the reacted melt composition as a function of decreasing melt–rock ratio are somewhat opposite for ABC- and BAC-bearing experiments (Figs 10 and 11). Whereas the overall trend for ABC-derived melts is to evolve towards less alkaline compositions with decreasing melt–rock ratio, the reverse is true for BAC-derived melts (as discussed above). This difference in the evolution of the reacted melts for the two starting melt compositions can be explained by the distinct silica and CO_2 concentrations of the two starting melts, using silica concentration as a proxy for degree of alkalinity or degree of silica-undersaturation. The silica content of ABC is very similar to that of KLB-1, which implies that the silica content of the bulk-rock mixture remains constant, irrespective of melt–rock ratio. Thus, the CO_2 concentration in the bulk melt–rock mixture dictates the degree of silica-undersaturation of the melt by lowering the SiO_2 concentration of the reacted melt (CO_2 being perfectly incompatible in the system and rate of melt consumption being constant, the CO_2 concentration of the bulk mixture is positively correlated with the CO_2 concentration in the reacted melt). Less CO_2 in the bulk melt–rock mixture or a lower melt–rock ratio implies lesser reduction of SiO_2 concentration owing to CO_2 content, hence producing a melt with a lower degree of silica-under-saturation than those produced at higher melt–rock ratios. On the other hand, BAC is more siliceous than peridotite; thus, a decreasing melt–rock ratio would indicate higher buffering capacity of silica concentration by peridotite in the melt–rock mixture. The CO_2 concentration in the melt–rock mixture being as low as it is (the highest being 1·3 wt % for the 50 wt % BAC-added run), the effect of bulk CO_2 on controlling the alkalinity of the melt is overridden by the SiO_2 concentration of the bulk melt–rock mixture, although the presence of dissolved CO_2 in the melt does cause the reacted melt to achieve a more silica-poor derivative composition
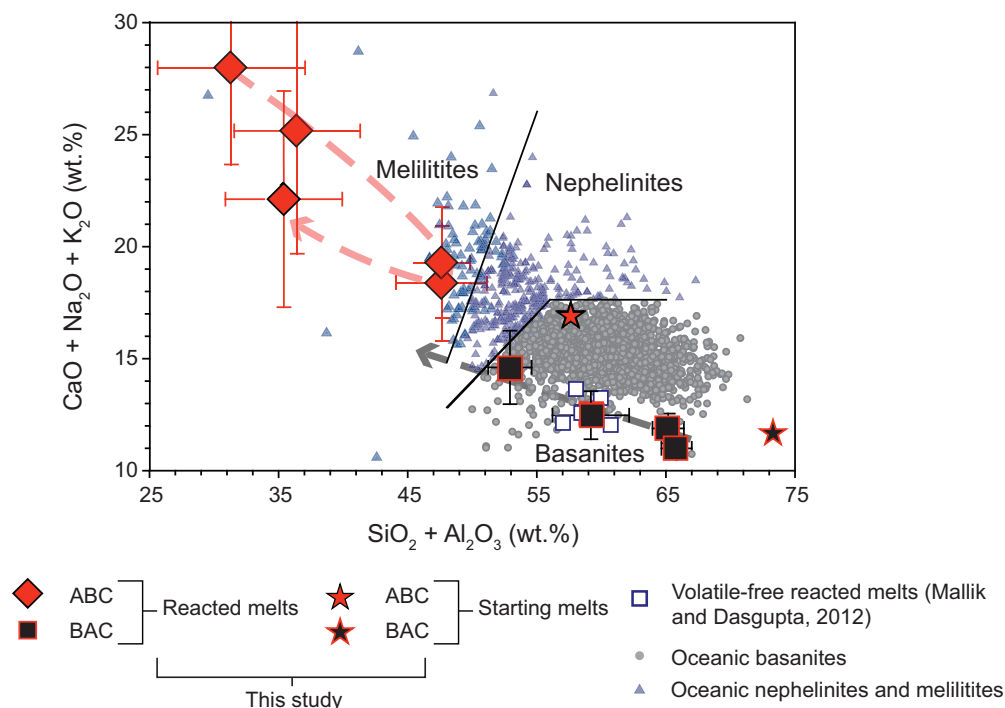
Fig. 10. Reacted melt and starting melt compositions from this study, volatile-free reacted melts from Mallik & Dasgupta (2012), and naturally occurring basanites, nephelinites and melilitites (data source given in the caption of Fig. 12) are plotted according to the melt alkalinity classification scheme of Le Bas (1989) The natural melts are categorized as basanites, nephelinites and melilitites according to their $SiO_2 + Al_2O_3$ (wt %) and $CaO + Na_2O + K_2O$ (wt %) concentrations. Symbols and error bars are the same as used in Fig. 4. The dashed arrows indicate the direction of evolution of melt compositions with decreasing melt–rock ratio during reaction.

compared with similar experiments in CO_2-free systems (Mallik & Dasgupta, 2012).

The contrasting evolution of the reacted melts for the two starting melt compositions is also evident when the melts are projected from Mg-Tschermak onto the plane Nepheline–Forsterite–Quartz (Fig. 11). The reacted melts have also been projected on the more commonly used Ca-Tschermak–Forsterite–Quartz plane from diopside following O'Hara (1968) (Supplementary Data Fig. S2). However, in the latter, the ABC-derived melts plot far outside the field of the plane of projection. Both KLB-1 and ABC plot on the Si-poor side of the thermal divide defined by the Ca-Tschermak–Enstatite join (Fig. 11 and Fig. S2). The reacted melts evolve to further Si-poor compositions and higher melt–rock ratio experiments (40 and 50 wt % melt-added runs) produce the most extreme Si-deficient compositions. Also, higher CO_2 concentrations in the source for increasing melt–rock ratios enhance precipitation of orthopyroxene at the liquidus via olivine consumption. This results in the residue of the melt–rock reaction evolving to a websteritic mineralogy at higher melt–rock ratios (as observed in Fig. 11, where the residue approaches the Ca-Tschermak–Enstatite boundary at higher melt–rock ratios). The simultaneous evolution of the reacted

melt and the residue gives rise to crossing tie-lines joining melt to residue composition via the bulk melt–rock mixture. On the other hand, for the BAC-derived experiments, BAC lying on the Si-rich side of the thermal divide results in the reacted melts varying from BAC-like compositions at higher melt–rock ratios (40 and 50 wt % BAC-added runs) to alkalic or relatively Si-poor melt compositions at intermediate melt–rock ratios (25 and 33 wt % BAC-added runs; Fig. 11 and Fig. S2). Simultaneously, more orthopyroxene crystallization occurs with increasing melt–rock ratio owing to the higher bulk SiO_2 concentrations and the residue thus evolves towards the thermal divide. In this scenario, the evolutionary trends of the reacted melts and those of the residues result in tie-lines that are mutually near-parallel for intermediate and high melt–rock ratios. Also, as noted by Mallik & Dasgupta (2012), melt–rock reaction between a siliceous melt and peridotite can result in a breach of the thermal divide by varying the melt–rock ratio in the bulk reacting lithology. The key observation in our study is that at intermediate melt–rock ratios, reacted, carbonated melts attain a higher degree of silica-undersaturation compared with their CO_2-free counterparts. Furthermore, the trend of compositional evolution of BAC-derived melts with decreasing melt–rock ratio (Fig. 11 and
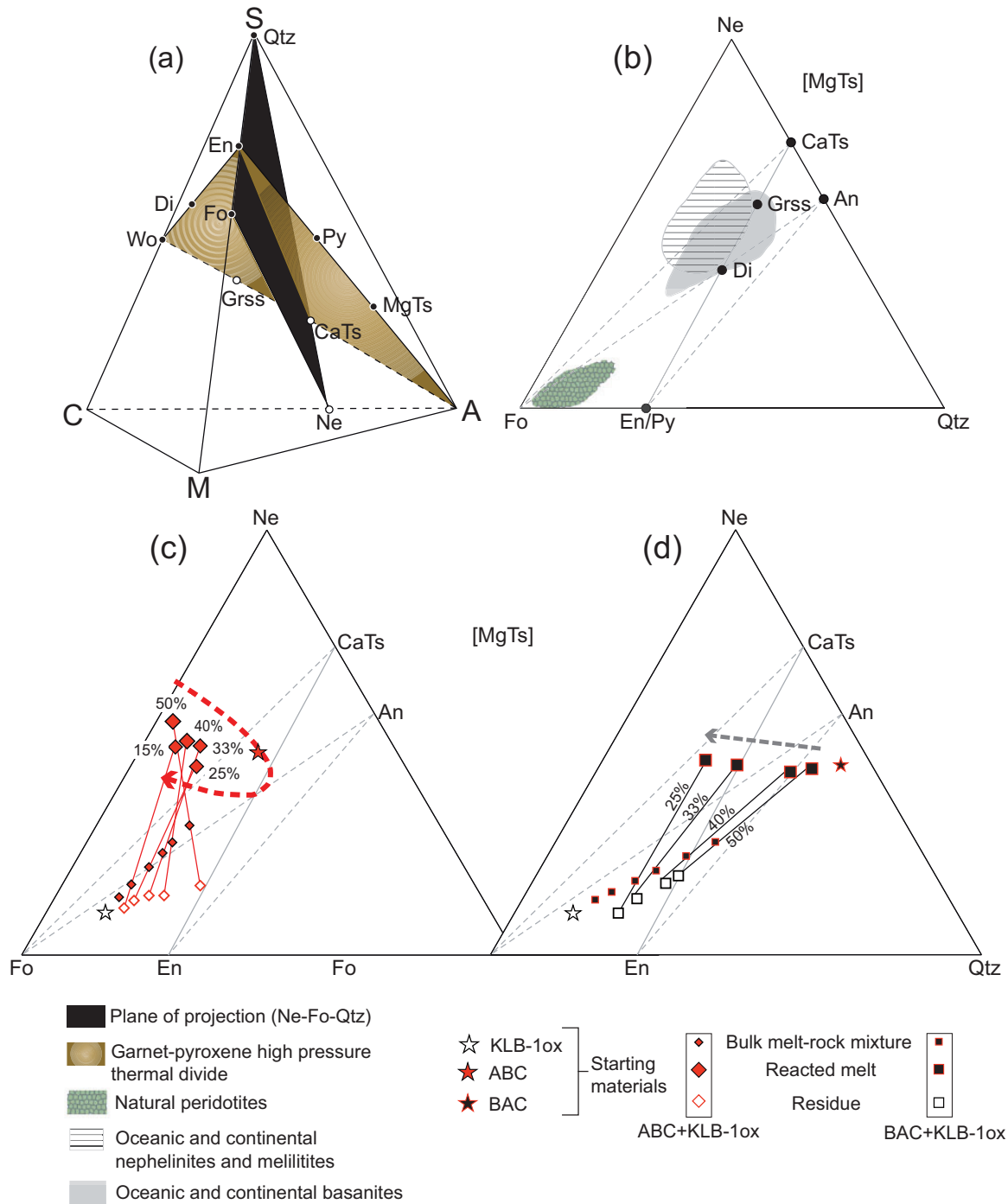
Fig. 11. (a) Pseudoternary plane nepheline–forsterite–quartz (Ne–Fo–Qtz) and the garnet–pyroxene high-pressure thermal divide of O'Hara & Yoder (1967) represented by wollastonite (Wo), enstatite (En), pyrope (Py), Mg-Tschermak (MgTs), Ca-Tschermak (CaTs) and grossular (Grss), plotted within the CMAS tetrahedron. The thermal divide intersects the pseudoternary plane at the CaTs–En join. (b) Projected compositions of the mineral end-members Ca-Tschermak (CaTs), anorthite (An), grossular (Grss), diopside (Di), enstatite (En) and pyrope (Py) on the pseudoternary plane along with fields for natural peridotites (GEOROC database), oceanic and continental basanites, nephelinites and melilitites (data sources in the caption of Fig. 12). The CaTs–En join represents the pyroxene–garnet thermal divide of O'Hara & Yoder (1967). (c, d) Starting material compositions (ABC, BAC, KLB-1ox) and bulk melt–rock mixture, reacted melt and residue compositions for l5 wt % to 50 wt % ABC-added runs and 25 wt % to 50 wt % BAC-added runs plotted in the pseudoternary system nepheline–forsterite–quartz (Ne–Fo–Qtz) projected from Mg-Tschermak (MgTs) according to O'Hara (1968). The percentage marked against each melt composition or tie-line indicates the amount of melt added to the melt–rock system. Tie-lines for each melt–rock ratio are constructed by joining the reacted melt and the residue compositions through the composition of bulk melt–rock mixture. The dashed arrows indicate the direction of decreasing melt–rock ratio corresponding to decreasing alkalinity in the case of ABC (c) and increasing alkalinity in the case of BAC (d). The projections were created using the software MetaRep (France & Nicollet, 2010).

Supplementary Data Fig. S2) suggests that low melt–rock ratios would probably result in even more silica-undersaturated magma compositions.

Genesis of alkalic oceanic basalts by eclogite melt–peridotite reaction in the presence of CO_2 and metasomatism of the mantle by CO_2-rich silicate melts

In Fig. 12, the reacted melts from this study (evolved from ABC and BAC) are plotted for comparison with reacted melts from volatile-free experiments (Mallik & Dasgupta, 2012), experimentally derived partial melts of carbonated and volatile-free peridotite, MORB-eclogite, natural oceanic basanites, nephelinites and melilitites [according to the classification of Le Bas (1989)], and the average HIMU OIB composition from Jackson & Dasgupta (2008). Also plotted are contours representing the frequency of sampled nephelinites and melilitites in compositional space. The MgO concentrations in the reacted melts derived from ABC do not vary significantly with melt–rock ratio (MgO decreases from 21 to 20 wt % with increasing melt–rock ratio); however, the MgO concentrations are higher than those of natural alkalic lavas. For a given MgO concentration, the reacted melts derived from partial reactive crystallization of ABC are extremely deficient in Al_2O_3 and too enriched in CaO and CaO/Al_2O_3 ratios to explain even the most extreme silica-undersaturated compositions such as melilitites. However, their SiO_2, TiO_2, FeO*, and Na_2O concentrations are within the range of some natural melilitites. Shallow-level olivine fractionation (as shown in Fig. 12) of up to 30 wt % will drive the reacted melt compositions towards lower MgO concentrations and concurrently towards slightly lower SiO_2, higher TiO_2, higher Al_2O_3, similar FeO* and higher Na_2O, and will not affect the CaO/Al_2O_3 of the melts. Thus, after 20% olivine fractionation, a typical reacted melt from ABC (as shown in Fig. 12) will be similar in composition to about 20–40% of natural silica-undersaturated lavas (nephelinites and melilitites) in terms of SiO_2 and CaO/Al_2O_3 and c. 60–80% of the same population in terms of TiO_2, Al_2O_3 and FeO. In terms of CaO and Na_2O there is a match with less than 20% of the nephelinite and melilitite population. Amongst the reacted melts, it is those at the lowest melt–rock ratios that can explain most of the natural nephelinites and melilitites the best, notably because of their higher SiO_2, higher Al_2O_3, lower CaO, lower Na_2O and lower CaO/Al_2O_3 compared with the reacted melts from higher melt–rock ratio experiments. Compositional modification by CO_2-exsolution and subsequent olivine fractionation are not the only processes that can modify the primary carbonated melt, however. Another possibility for the compositional evolution of carbonated silicate melt upon ascent is immiscible separation into a carbonatite and a

silica-undersaturated melt as has been demonstrated in natural occurrences and by experiments in several studies (e.g. Koster Van Groos & Wyllie, 1966; Church & Jones, 1995; Lee & Wyllie, 1997; Gerbode & Dasgupta, 2010). If ABC-derived melts enter a miscibility gap at shallower depths and perhaps lower temperatures, their extreme enrichments in CaO and depletion in SiO_2 may be moderated. Therefore, although ABC-derived reacted melts at mantle conditions are all melilititic, immiscibility may also cause such melts to give rise to less extreme basanite or alkali basalt compositions.

From Fig. 12, it can be observed that the reacted melts from BAC (those derived from intermediate melt–rock ratios) are by themselves a good match for some of the Mg-rich (MgO >12–15 wt %) natural nephelinites in terms of SiO_2, Al_2O_3, FeO*, CaO, Na_2O and CaO/Al_2O_3. However, most erupted, alkalic OIB (greater than 80% of nephelinites and melilitites) have MgO <15 wt %, suggesting that olivine fractionation is a viable mechanism for these reacted melts to generate alkalic OIB. Olivine fractionation of around 20 wt % drives the melt composition towards lower MgO, slightly lower SiO_2 and FeO*, higher Al_2O_3, CaO and Na_2O, and constant CaO/Al_2O_3. As a result of about 10% olivine fractionation from a typical reacted melt from BAC (as shown in Fig. 12), the melt will match the composition of 60–80% of nephelinites and melilitites in terms of SiO_2, Al_2O_3, CaO, Na_2O and CaO/Al_2O_3 and about 20–40% of the population in terms of FeO*. Overall, the most significant improvements of the involvement of CO_2 over volatile-free conditions in the eclogite melt–lherzolite reaction are lowering of SiO_2 and Al_2O_3, and elevation of FeO*, Na_2O and CaO/Al_2O_3, for a given MgO content, resulting in a better match with natural nephelinites and transitional nephelinitic basanites sampled. The TiO_2 concentrations of these reacted melts are significantly higher (5·9–6·4 wt %) than those of natural alkalic basalts and increase even further upon olivine fractionation. However, as mentioned by Mallik & Dasgupta (2012), such enrichment in TiO_2 can be diluted by mixing with depleted peridotite partial melts. A mixing trend is plotted in Fig. 12 between a typical reacted melt derived from BAC and a carbonated peridotite partial melt generated at 1375°C, 3 GPa (Dasgupta *et al.*, 2007); that is, the same temperature–pressure conditions at which the reacted melt was generated. It is evident that mixing of carbonated peridotite-derived melt with the reacted melt from BAC in a 3:2 ratio will produce a melilitite and drive the mixture towards a lower TiO_2 concentration and a slightly higher MgO concentration compared with the reacted melt from BAC. Furthermore, such a product of melt–melt mixing upon olivine crystallization can produce melilitites representative of at least 40% of the sampled population or can form a less extreme basanite composition upon immiscible separation. The reacted
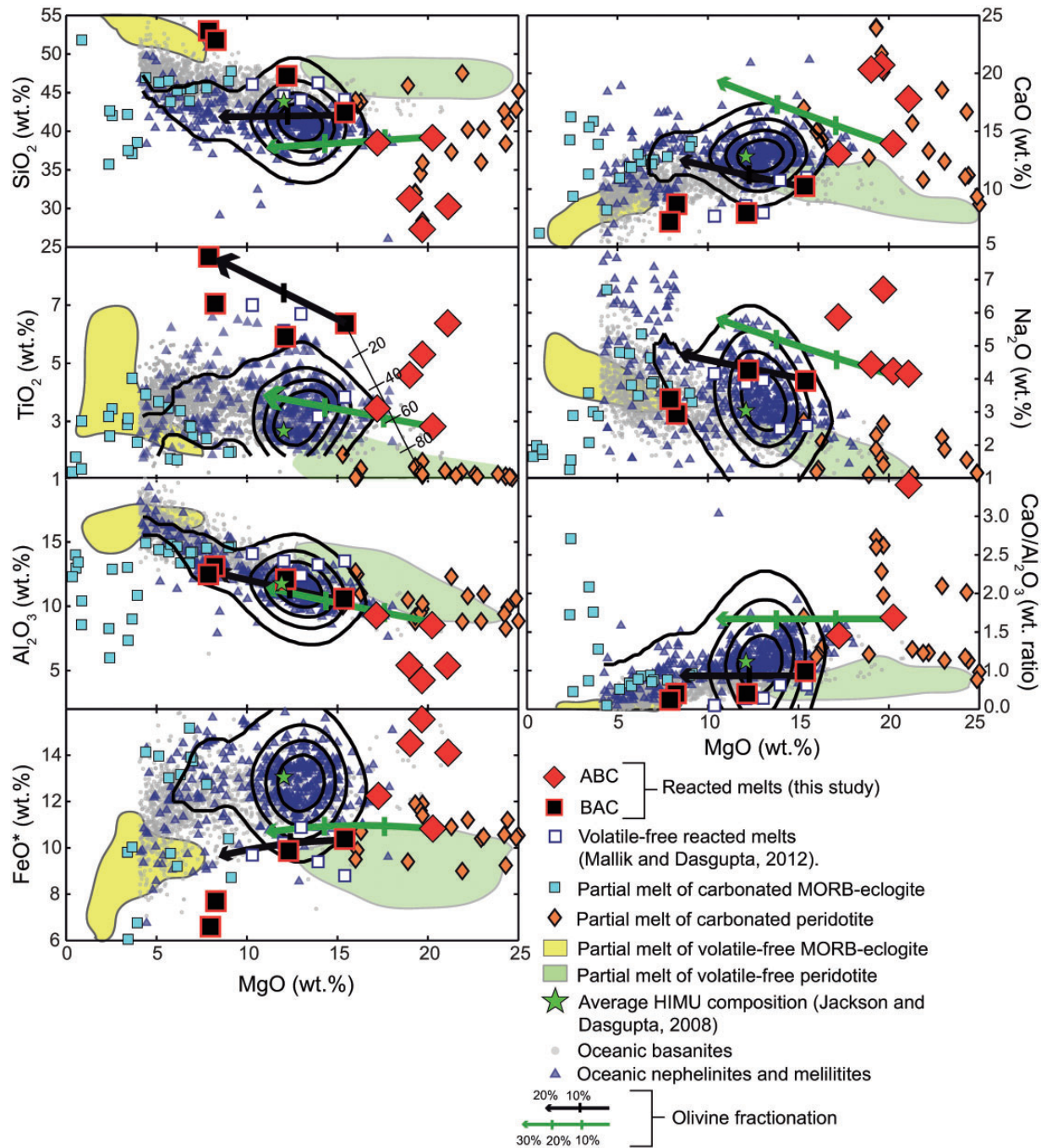
Fig. 12. Major element concentrations of reacted melts from this study (owing to partial reactive crystallization of ABC and BAC), volatile-free reacted melts from Mallik & Dasgupta (2012), experimentally derived partial melts of carbonated MORB-eclogite (Hammouda, 2003; Gerbode & Dasgupta, 2010; Kiseeva *et al.*, 2012), partial melts of carbonated peridotite (Hirose, 1997; Dasgupta *et al.*, 2007), partial melts of volatile-free MORB-eclogite (Pertermann & Hirschmann, 2003; Spandler *et al.*, 2008), partial melts of volatile-free peridotite from 2·5 to 4·5 GPa (Takahashi, 1986; Hirose & Kushiro, 1993; Walter, 1998; Longhi, 2002; Davis *et al.*, 2011) and the average HIMU OIB composition (Jackson & Dasgupta, 2008) plotted as a function of MgO concentration in the melt. The experimental melts are compared with naturally occurring oceanic basanites, nephelinites and melilitites (GEOROC database; Duprat *et al.*, 2007; Barker *et al.*, 2009; Takamasa *et al.*, 2009; Aulinas *et al.*, 2010; Dyhr & Holm, 2010; Martins *et al.*, 2010; Mourão *et al.*, 2010; Torres *et al.*, 2010; Kawabata *et al.*, 2011; de Ignacio *et al.*, 2012). Frequency contours (black curves) for nephelinites and melilitites were constructed at intervals of 20% from 80% (innermost contour) to 20% (outermost contour) using a MATLAB function SMOOTHHIST2D.m (Perkins, 2006). Olivine fractionation correction of 30% is shown for an MgO-rich, ABC-derived melt (G239) and of 20% for an MgO-rich BAC-derived melt (G221) using $k_D^{Fe^*-Mg^*}$ (ol–melt) = 0·3 (Roeder & Emslie, 1970). No significant difference in olivine-fractionation trends were observed using $k_D^{Fe^*-Mg^*}$ (ol–melt) = 0·34 (Matzen *et al.*, 2011); hence, these trends were not plotted for clarity. In the MgO vs TiO$_2$ plot, a mixing line is shown between an MgO-rich BAC-derived melt (B222) and a partial melt of carbonated peridotite to demonstrate the TiO$_2$ concentration of the melt–melt mixture. The numbers next to the tick marks represent the percentage of carbonated peridotite partial melt to be added to the BAC-derived melt.
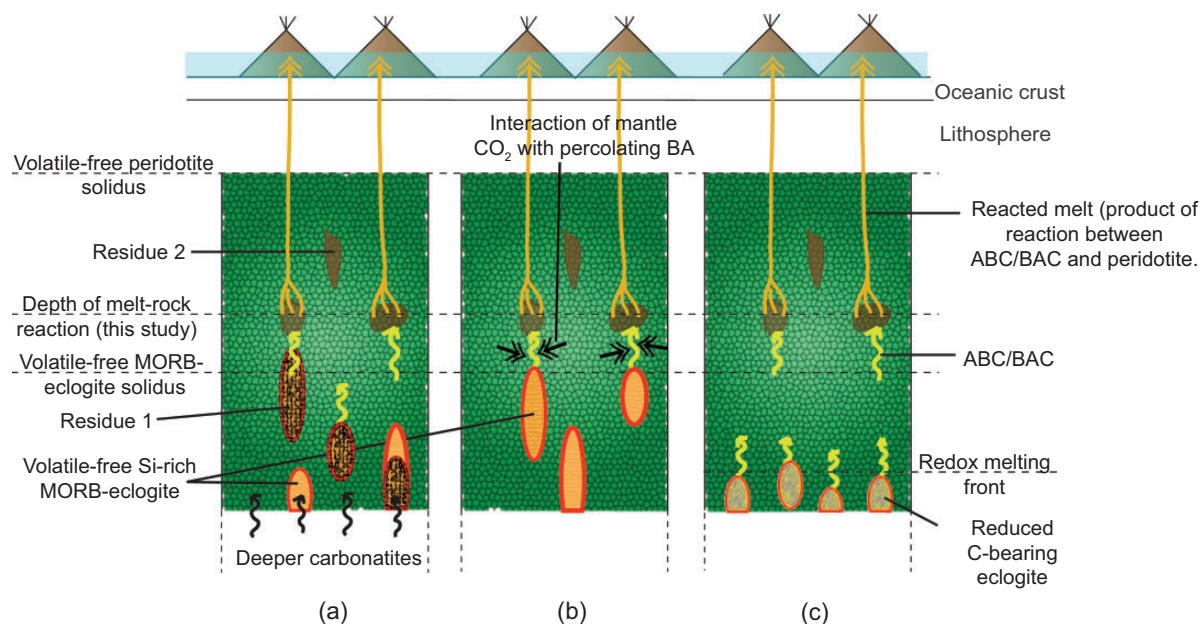
Fig. 13. Schematic illustration demonstrating three ways in which ABC- and BAC-like melts may be generated in the Earth's mantle followed by reaction of the melt with peridotite to produce reacted melts erupting as alkalic lavas and leaving behind a garnet-websterite (± olivine) residue ('Residue 2'). (a) Carbonatitic melts produced by deep, low-degree melting or redox-melting of carbon-bearing eclogite or peridotite infiltrate into volatile-free, SiO_2-rich MORB-eclogite to produce a carbonated silicate melt and 'Residue 1'. Whether the carbonated silicate melt produced is ABC-like or BAC-like depends on the ratio of carbonatite to MORB-eclogite—a higher ratio would favor formation of melt similar in composition to ABC (Gerbode & Dasgupta, 2010), whereas a lower ratio would favor a melt composition closer to BAC. (b) Recycled volatile-free Si-rich MORB-eclogite, upon partial melting during upwelling, generates a basaltic andesite melt (volatile-free) and this melt scavenges CO_2 from the background mantle or from a carbonatitic melt producing a BAC-like melt composition. (c) A third scenario where MORB-eclogite pods containing reduced carbon at depth, upon upwelling, undergo redox melting and produce carbonated silicate melt at the redox front solidus. In this scenario production of eclogite-derived, carbonated, silicate melt would not require carbonatite–eclogite reaction and redox melting-induced carbonated silicate melt can directly infiltrate the peridotite (this study). The depth of the redox melting front is not constrained as yet for carbon-bearing eclogitic systems and it is also uncertain whether redox melting of carbon-bearing eclogite will produce a carbonated silicate melt or a carbonatitic melt. However, by analogy with peridotitic systems where the depth of the transition from carbonatitic melt to carbonated silicate melt is fairly deep, direct generation of a carbonated silicate melt at a similar redox front is expected (Dasgupta *et al.*, 2013). It is plausible that redox melting of a diamond- or graphite-bearing eclogite also directly produces a carbonated silicate melt. In this scenario, the first-stage melt–rock reaction will be that between an ABC-like melt and peridotite.

melts derived from high melt–rock ratios of BAC lack sufficient MgO ($<$10 wt %) to be considered primary magmas. However, this also implies that these melts can be viable metasomatic agents in the mantle as discussed below. The melts generated through partial reactive crystallization of an original eclogite melt in a peridotite matrix in this study are a significant improvement over the deficiencies of TiO_2 and MgO in peridotite and eclogite-derived partial melts respectively, in explaining the majority of natural alkalic basalts.

Dynamic scenario of eclogite-derived carbonated silicate melt and peridotite reaction

Possible scenario of genesis of eclogite-derived carbonated silicate melts

The first consideration for the melt–rock reaction scenario explored here is the generation of carbonated MORB-eclogite partial melts. If the mantle is locally oxidized at depth, carbonated MORB-eclogite will encounter its

carbonatite-generating solidus in an upwelling, convective mantle with $T_P = 1350°C$ at around 360 km (11 GPa), whereas the solidus will be located even deeper (i.e. $\sim$460 km; $<$14 GPa) in a mantle with $T_p = 1550°C$ (Dasgupta *et al.*, 2004, 2007; Litasov & Ohtani, 2010). Incipient melting at the solidus, in this case, will generate a carbonatitic melt (Hammouda, 2003; Dasgupta *et al.*, 2004, 2005; Gerbode & Dasgupta, 2010; Litasov & Ohtani, 2010; Kiseeva *et al.*, 2012), which, owing to its extreme mobility (Minarik & Watson, 1995; Hammouda & Laporte, 2000), should leave the parent eclogite body efficiently. It is thus difficult to envision how a high melt fraction, carbonated silicate melt of MORB-eclogite could be generated at 3 GPa, 1375°C, the condition under which eclogitic partial melt and lherzolite reaction is studied here. The genesis of a carbonated silicate melt such as ABC or BAC can be explained by the following scenario discussed at length by Dasgupta *et al.* (2006, 2007) and Gerbode & Dasgupta (2010). Silica-saturated carbonated MORB-eclogite (coesite or stishovite-eclogite at the

conditions of near-solidus melting), upon partial melting at low degrees, can produce immiscible carbonatitic and silica-rich melts (Gerbode & Dasgupta, 2010; Kiseeva *et al.*, 2012). The immiscible silica-rich melts may have characteristics similar to our BAC or ABC composition, depending on the bulk compositions of interest. Perhaps more realistically, the carbonate-rich melt derived from carbonated peridotite (e.g. Falloon & Green, 1989; Dasgupta & Hirschmann, 2006; Dasgupta *et al.*, 2013) or deeply subducted carbonated eclogite (e.g. Dasgupta *et al.*, 2004; Yaxley & Brey, 2004) or carbonated pelite (e.g. Grassi & Schmidt, 2011; Tsuno *et al.*, 2012) has the potential to metasomatize the surrounding mantle. Reactive processes involving carbonatite and volatile-free MORB-eclogite can produce a wide range of carbonated silicate melt compositions depending on the carbonate melt:MORB-eclogite ratio. If the carbonate melt fraction is rather high, at least locally, such interaction would probably produce a carbonated silicate melt similar in composition to ABC (Gerbode & Dasgupta, 2010; Fig. 13a). On the other hand, if the interaction volume is carbonate-poor, a MORB-eclogite partial melt may dissolve some carbonate with very little impact on its major element chemistry (i.e. a composition similar to BAC; Fig. 13a). BAC can also form if an 8% melt of volatile-free MORB-eclogite reacts with percolating carbonatite, carbonated silicate melt and/or CO_2-rich fluid (Fig. 13b).

Whereas generation of carbonated silicate melt of MORB-eclogite (ABC and/or BAC) in an oxidized mantle will require a reactive process as outlined above, such melts may also be generated by direct decompression melting of graphite- or diamond-bearing eclogite, at a redox front. In fact, this mechanism may be more likely, given the current understanding of the oxygen fugacity profile of the Earth's mantle as a function of depth (e.g. Stagno *et al.*, 2013). For example, if the upper mantle reaches Fe–Ni metal saturation at depths (e.g. Rohrbach *et al.*, 2007, 2011), the carbonatite-generating solidus of carbonated eclogite may not apply. Metal saturation for peridotitic upper mantle has been shown to occur at ∼250 km depth (Rohrbach *et al.*, 2007, 2011), but a similar metal precipitation condition for eclogitic bulk compositions is not constrained as yet. If the transition from carbonatite to carbonated silicate melt for eclogite is fairly deep, as shown to be the case for peridotitic systems (Dasgupta *et al.*, 2013), then redox melting of reduced carbon-bearing eclogite at the solidus may directly produce a carbonated silicate melt (Fig. 13c).

Scenario and conditions of MORB-eclogite-derived carbonated silicate melts and fertile peridotite reaction in the upper mantle

Once the carbonated silicate melt is generated by equilibration of carbonatite or CO_2-rich fluid and

Table 9: Summary of descriptive statistics (mean, standard deviation and median) of composition of oceanic and continental nephelinites and melilitites

		Continental			Oceanic			Relative difference (%)
		Mean	SD	Median	Mean	SD	Median	
Nephelinites				$n = 348$			$n = 274$	
	SiO_2	42·4	1·6	42·3	42·0	1·8	41·7	1·3
	TiO_2	3·1	0·9	3·0	3·5	0·9	3·4	−14·0
	Al_2O_3	12·3	2·2	11·9	12·3	1·8	11·9	0·3
	FeO*	12·1	2·1	12·0	12·7	1·5	12·6	−5·7
	MgO	10·6	3·6	10·6	11·2	3·1	12·2	−15·1
	CaO	13·3	1·9	13·4	12·6	1·6	12·6	5·8
	Na_2O	3·8	1·2	3·7	3·8	1·4	3·5	4·4
Melilitites				$n = 332$			$n = 95$	
	SiO_2	38·9	2·6	38·8	38·4	4·9	39·1	−0·8
	TiO_2	3·6	1·3	3·1	3·8	1·3	3·7	−20·2
	Al_2O_3	9·5	1·8	9·4	10·7	2·4	10·5	−11·8
	FeO*	12·1	2·5	12·0	13·7	2·7	13·1	−9·0
	MgO	13·9	5·3	15·5	13·1	2·3	13·3	14·4
	CaO	16·0	2·8	15·9	14·5	2·9	13·7	13·6
	Na_2O	3·4	2·1	3·0	3·6	1·2	3·4	-10·8

Relative difference (%) = [median (continental) – median (oceanic)]/median (continental) × 100.
*All Fe assumed to be FeO.

MORB-eclogite or by redox melting of carbon-bearing eclogite, the melt will move away from the eclogite bodies and encounter peridotite over a range of depth–temperature conditions. The experiments presented here capture such interactions at the base of a mature lithosphere, at ∼100 km and 1375°C; that is, proximal to the ocean island basalt source region. On the scale of the entire OIB source region the effective melt:rock ratio of such reaction is expected to be low, but on local (i.e. meter to tens of meters) scale the melt:rock ratio can be as high as those explored in our experiments. After carbonated eclogite melt–peridotite reaction, the reacted melts have the potential to segregate from the source region along channels. Otherwise, these alkalic melts can be potential metasomatizing agents within the mantle in accordance with studies that have proposed CO_2-rich silicate melts metasomatizing the oceanic mantle (e.g. Gregoire *et al.*, 2000; Delpech *et al.*, 2004). However, it should be noted that the nature of metasomatism will evolve continuously during the ascent of the melt through the mantle, because after each stage of melt–rock reaction the melt composition will evolve to become more silica-undersaturated than in the previous
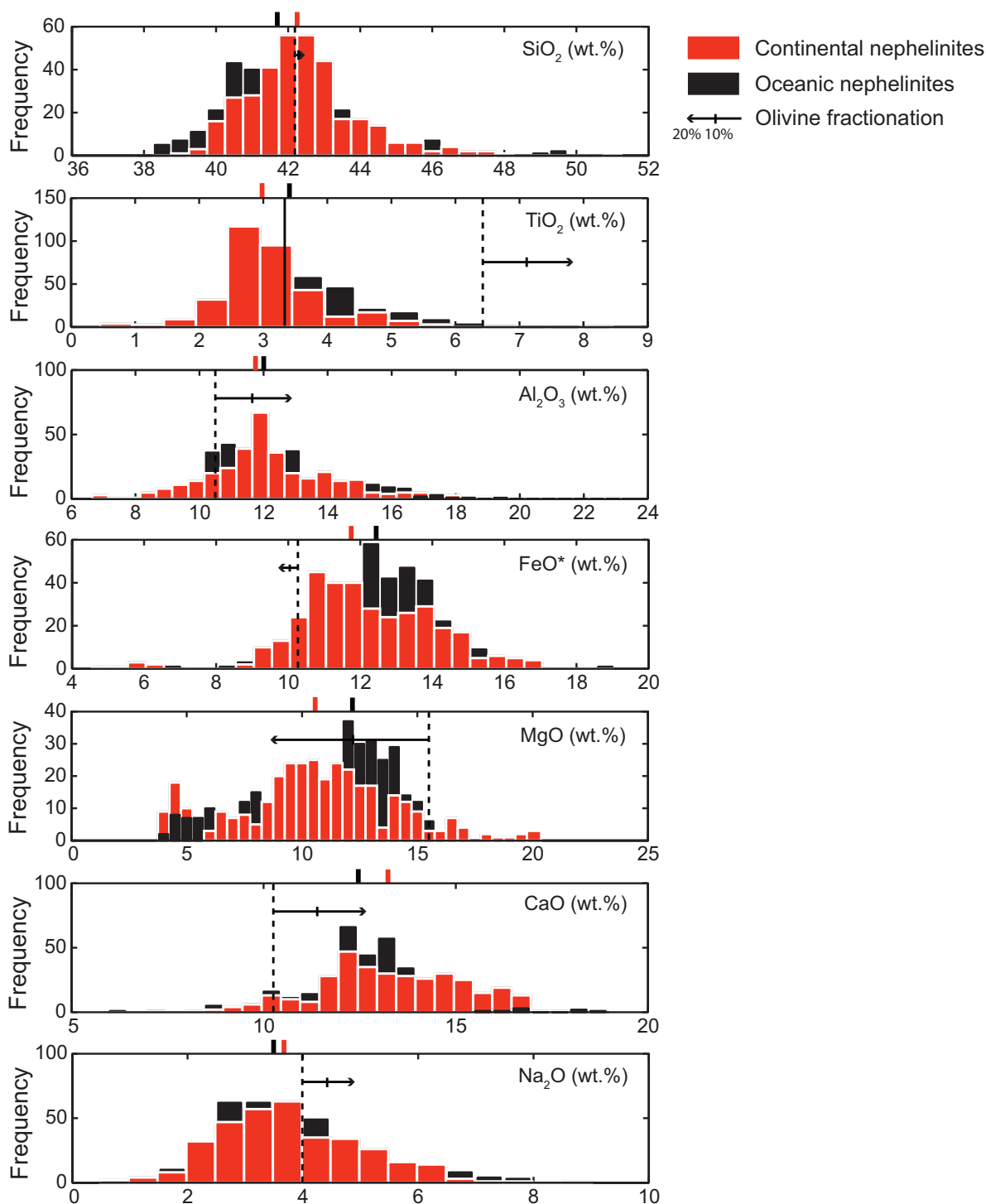
Fig. 14. Histograms of major element concentrations (oxide wt %) in oceanic and continental nephelinites. Bin intervals and sizes are the same for the two datasets in a single composition vs frequency sub-plot. Frequency represents the absolute number of data points present in a bin. The two colored tick marks (non-black for continental; black for oceanic) at the top of each sub-plot represent the median composition of the respective dataset (reported in Table 9). Natural nephelinites are compared with reacted melt from the 25% BAC-added experiment because this reacted melt is a nephelinitic basanite according to the classification of Le Bas (1989) (Fig. 10). The melt composition derived from the 25% BAC-added experiment (B222) is plotted on each histogram with a dashed line. Vectors of change in melt composition owing to olivine fractionation of up to 20 wt % are also shown by black arrows with ticks on them representing 10 wt % olivine fractionation. The continuous black line in the TiO_2 histogram represents the composition of the 3:2 mixture of carbonated peridotite partial melt and reacted melt from the 25% BAC-added experiment. Data sources used for oceanic nephelinites are given in the caption of Fig. 12. Data for continental nephelinites are from the GEOROC database, Pilet *et al.* (2002), Ho *et al.* (2003), Chashchin *et al.* (2007), Zeng *et al.* (2010), Melluso *et al.* (2011) and Tschegg *et al.* (2011).

stage. Furthermore, as discussed above, the reacted melt may evolve not only by crystal fractionation and CO_2-degassing, but also by liquid immiscibility. One noteworthy corollary of our experimental results is that high-MgO melts [as high as 15 wt % (BAC-derived) to 21 wt % (ABC-derived) on a CO_2-free basis at low to intermediate melt:rock ratios] with many compositional attributes similar to alkalic OIB are generated by reaction of low-MgO eclogitic melts and fertile peridotite, below the volatile-free peridotite solidus. We note that the involvement of dissolved carbonates makes the melt even more MgO rich compared with other similar bulk compositions at CO_2-free conditions (Mallik & Dasgupta, 2012). If the P–T conditions of our experiments are projected to a plausible solid mantle adiabat, a mantle potential temperature no more than 1350°C is necessary. Therefore, our experiments suggest that if eclogite partial melt–peridotite reaction and the possible compositions of derivative magmas are not taken into account, the temperatures of primary melilititic to nephelinitic basanite magmas can be significantly overestimated. Our data thus suggest that such intraplate magmatism can be generated in 'colder regions' of the mantle with 'normal potential temperatures' such as along the periphery of a thermal plume, in regions of small-scale convection beneath the lithosphere, and other instabilities such as weak thermal anomalies (e.g. Raddick *et al.*, 2002; Ballmer *et al.*, 2007).

Eclogite-derived carbonated melt–peridotite interaction beneath continents

The scenario of melt–rock reaction and mantle metasomatism captured in our experiments is also relevant beneath continental lithosphere where stacked subducted carbonated MORB-eclogite may undergo partial melting (e.g. Heaman *et al.*, 2002; Kiseeva *et al.*, 2012) and melt–rock reaction such as documented in this study may occur. In fact, metasomatism of continental lithospheric mantle by carbonate-bearing melts or fluids has been shown by several studies (e.g. Dautria *et al.*, 1992; Ionov *et al.*, 1996; Yaxley *et al.*, 1998; Kamenetsky *et al.*, 2004). In terms of composition, comparison between oceanic and continental suites of nephelinites–melilitites demonstrate that even though they largely overlap in composition, there are differences in the median values of certain compositional parameters. Nephelinites from continents are 14%, 6% and 15% lower (relative) in median TiO_2, FeO* and MgO, respectively, and 6% higher in CaO compared with those found in oceanic settings (Table 9; Fig. 14). Melilitites display the greater difference in composition between the two settings. Continental melilitites are 20%, 12%, 9% and 11% (relative) depleted in median compositions of TiO_2, Al_2O_3, FeO* and Na_2O, respectively as well as 14% enriched in MgO and CaO compared with oceanic melilitites (Table 9; Fig. 15).

In Fig. 14, the nephelinitic basanite derived from BAC is compared with continental nephelinites. Although the reacted melts are more MgO-rich, and CaO- and Al_2O_3-poor, than the majority of continental nephelinites, 10–20% olivine fractionation produces a good match with the nephelinites around the median population. The experimental reacted melt is close to the median population of continental nephelinites in terms of SiO_2 and Na_2O, and 10–20 wt % olivine fractionation can explain a significant proportion of continental nephelinites. The reacted melts are more enriched in TiO_2 than the median concentration in continental nephelinites by >3 wt % and olivine fractionation only results in further enrichment of TiO_2, and hence increased departure from the median concentration. However, as shown in Fig. 14, mixing of the reacted melt with TiO_2-poor peridotite-derived partial melts can drive the resultant reacted melt towards the major population of natural nephelinites.

In Fig. 15, the melilititic melts derived from ABC are compared with continental melilitites. The reacted melts at intermediate melt–rock ratios provide the best match for the majority of continental melilitites. These experimentally derived melts are compositionally close to the median population of continental melilitites in terms of SiO_2, TiO_2 and FeO*. The reacted melts are Al_2O_3 and CaO-poor and MgO- and Na_2O-rich compared with the median population of natural lavas. Approximately 10–15 wt % olivine fractionation improves the match of the reacted, ABC-derived melts with the majority of continental melilitites in terms of Al_2O_3, MgO and CaO.

CONCLUSIONS

We demonstrate that reaction between a carbonated alkalic basalt (ABC) and peridotite generates reacted melts of melilititic composition with the degree of alkalinity decreasing with decreasing melt–rock ratio. On the other hand, a carbonated basaltic andesite (BAC) generates silica-poor basanites or nephelinitic basanites (as opposed to more siliceous basanites in volatile-free conditions; Mallik & Dasgupta, 2012) upon partial reactive crystallization in a peridotitic matrix, and the degree of alkalinity increases with decreasing melt–rock ratio. The trend of reacted melt compositions as a function of melt–rock ratio suggests that similar reactions at lower melt–rock ratios would result in true nephelinitic melt compositions. Whereas the reacted melts derived from ABC at lower melt–rock ratios match the major element compositions of some oceanic melilitites, the reacted melts from BAC are excellent matches with oceanic nephelinites and transitional basanites in terms of SiO_2, Al_2O_3, FeO*, CaO, Na_2O and CaO/Al_2O_3. These reacted melts can either erupt by themselves or act as potential metasomatic agents in the Earth's mantle. Our study underscores the importance of reactive infiltration of
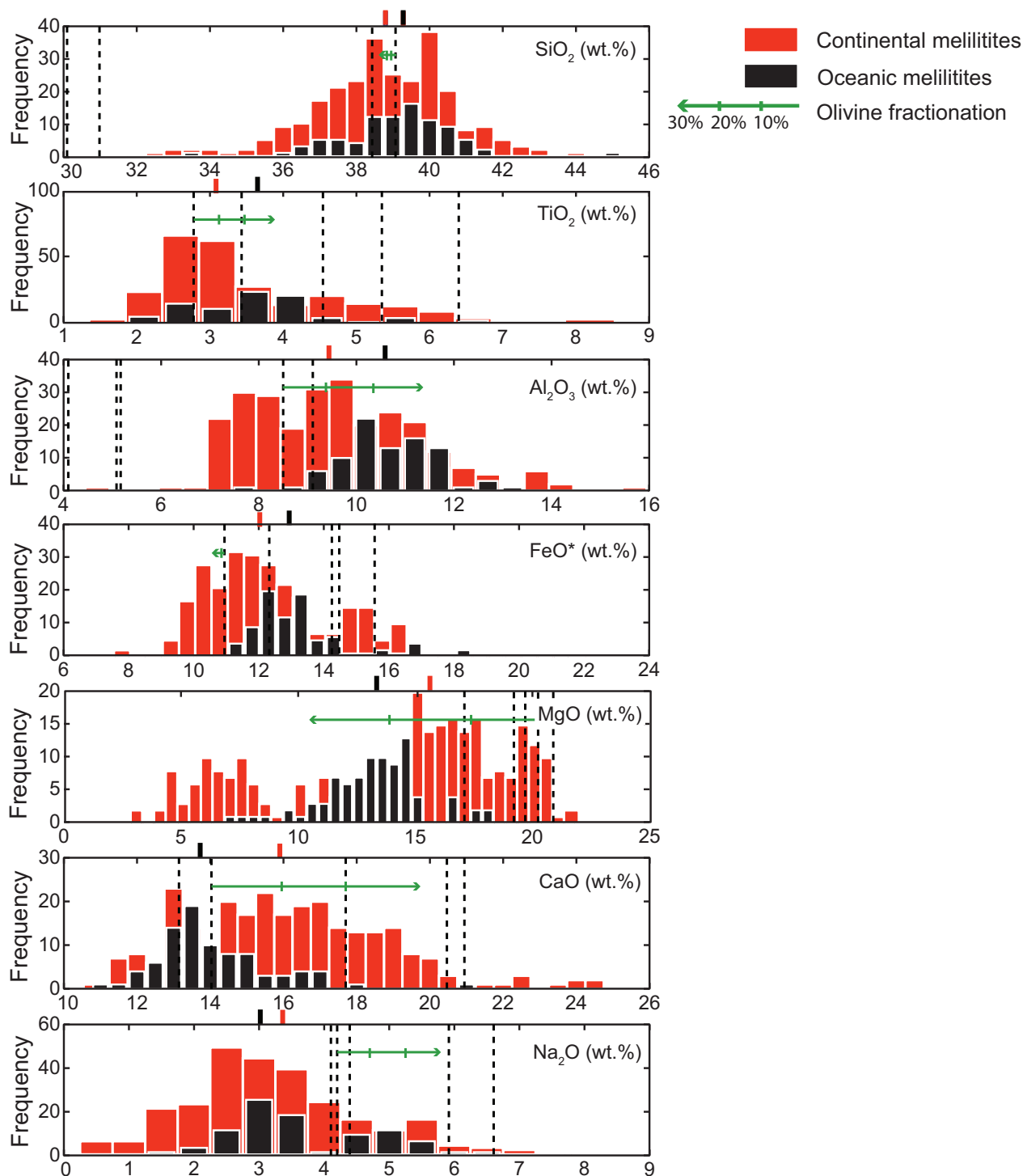
Fig. 15. Histogram of major element concentrations (oxide wt %) in oceanic and continental melilitites. Bin intervals and sizes are the same for the two datasets in a single composition vs frequency histogram. Frequency represents the absolute number of data points present in a bin. The two colored tick marks at the top of each sub-plot (non-black for continental; black for oceanic) represent the median composition of the respective dataset (reported in Table 9). The melilititic melt compositions derived from all ABC-added experiments (Fig. 10) are plotted on each histogram with dashed black lines, except for the SiO_2 frequency plot, where the reacted melt from the 50 wt % ABC-added run lies outside the range of concentrations displayed (towards the lower concentration end). Vectors of change in melt composition owing to olivine fractionation of up to 30 wt % are shown by arrows with ticks on them representing 10 and 20 wt % olivine fractionation. The olivine fractionation correction is shown for the reacted melt corresponding to the 25% ABC-added run (the same melt composition for which the fractionation correction is shown in Fig. 12). Data for continental melilitites are from the GEOROC database, Brey (1978), Frey *et al*. (1978), Dawson *et al*. (1995), Hegner *et al*. (1995), Wilson *et al*. (1995), Nielsen *et al*. (1997), Ivanikov *et al*. (1998), Janney *et al*. (2002), Schultz *et al*. (2004) and Melluso *et al*. (2011).

crustal melts into peridotite in the genesis of a wide range of basaltic compositions. In particular, our experiments demonstrate that if reactive processes involving MORB-like crust and peridotite are considered in the presence of trace CO_2, the majority of the major element compositional attributes of silica-poor basalts can be explained. Reacted carbonated silicate melts in MORB-eclogite–peridotite systems are reasonable primary magma candidates for both ocean island melilitites–nephelinites–basanites and continental nephelinites–melilitites. Therefore, the dominant form of heterogeneity in the distal source regions of ocean island basalts can be silica-saturated MORB-eclogite (i.e. subducted oceanic crust), and consideration of high-MgO, silica-poor garnet pyroxenite or eclogite in the generation of alkalic basalts is not necessary. Furthermore, low-MgO eclogite partial melts by partial reactive crystallization can evolve to high-MgO, silica-poor magmas at ambient mantle temperatures. Thus generation of silica-undersaturated alkalic basalts in intraplate settings does not require excess mantle potential temperatures and such magmas can form along the periphery of strong plume, in a weak plume, and by decompression in the ambient mantle caused by small-scale convection.

ACKNOWLEDGEMENTS

FUNDING

SUPPLEMENTARY DATA

Supplementary data for this paper are available at *Journal of Petrology* online.

REFERENCES

Aulinas, M., Gimeno, D., Fernandez-Turiel, J. L., Font, L., Perez-Torrado, F. J., Rodriguez-Gonzalez, A. & Nowell, G. M. (2010). Small-scale mantle heterogeneity on the source of the Gran Canaria (Canary Islands) Pliocene–Quaternary magmas. *Lithos* **119**, 377–392.

Ballmer, M. D., van Hunen, J., Ito, G., Tackley, P. J. & Bianco, T. A. (2007). Non-hotspot volcano chains originating from small-scale sublithospheric convection. *Geophysical Research Letters* **34**, doi:10.1029/2007gl031636.

Barker, A. K., Holm, P. M., Peate, D. W. & Baker, J. A. (2009). Geochemical stratigraphy of submarine lavas (3–5 Ma) from the Flamengos Valley, Santiago, southern Cape Verde Islands. *Journal of Petrology* **50**, 169–193, doi:10.1093/petrology/egn081.

Brey, G. (1978). Origin of olivine melilitites—chemical and experimental constraints. *Journal of Volcanology and Geothermal Research* **3**, 61–88.

Brey, G. & Green, D. H. (1975). The role of CO_2 in the genesis of olivine melilitite. *Contributions to Mineralogy and Petrology* **49**, 93–103, doi:10.1007/bf00373853.

Brey, G. & Green, D. H. (1977). Systematic study of liquidus phase relations in olivine melilitite $+H_2O$ $+CO_2$ at high pressures and petrogenesis of an olivine melilitite magma. *Contributions to Mineralogy and Petrology* **61**, 141–162, doi:10.1007/bf00374364.

Brey, G. P. & Kohler, T. (1990). Geothermobarometry in four-phase lherzolites II. New thermobarometers, and practical assessment of existing thermobarometers. *Journal of Petrology* **31**, 1353–1378, doi:10.1093/petrology/31.6.1353.

Brooker, R. A. (1998). The effect of CO_2 saturation on immiscibility between silicate and carbonate liquids: an experimental study. *Journal of Petrology* **39**, 1905–1915, doi:10.1093/petroj/39.11-12.1905.

Brooker, R. A., Kohn, S. C., Holloway, J. R. & McMillan, P. F. (2001). Structural controls on the solubility of CO_2 in silicate melts: Part I: bulk solubility data. *Chemical Geology* **174**, 225–239, doi:10.1016/S0009-2541(00)00353-3.

Chase, C. G. (1981). Oceanic island Pb: two-stage histories and mantle evolution. *Earth and Planetary Science Letters* **52**, 277–284.

Chashchin, A., Martynov, Y., Rasskazov, S., Maksimov, S., Brandt, I. & Saranina, E. (2007). Isotopic and geochemical characteristics of the late Miocene subalkali and alkali basalts of the southern part of the Russian Far East and the role of continental lithosphere in their genesis. *Petrology* **15**, 575–598, doi:10.1134/s0869591107060045.

Church, A. A. & Jones, A. P. (1995). Silicate—carbonate immiscibility at Oldoinyo Lengai. *Journal of Petrology* **36**, 869–889, doi:10.1093/petrology/36.4.869.

Dasgupta, R. & Hirschmann, M. M. (2006). Melting in the Earth's deep upper mantle caused by carbon dioxide. *Nature* **440**, 659–662, doi:10.1038/nature04612.

Dasgupta, R., Hirschmann, M. M. & Withers, A. C. (2004). Deep global cycling of carbon constrained by the solidus of anhydrous, carbonated eclogite under upper mantle conditions. *Earth and Planetary Science Letters* **227**, 73–85.

Dasgupta, R., Hirschmann, M. & Dellas, N. (2005). The effect of bulk composition on the solidus of carbonated eclogite from partial melting experiments at 3 GPa. *Contributions to Mineralogy and Petrology* **149**, 288–305, doi:10.1007/s00410-004-0649-0.

Dasgupta, R., Hirschmann, M. M. & Stalker, K. (2006). Immiscible transition from carbonate-rich to silicate-rich melts in the 3 GPa melting interval of eclogite $+ CO_2$ and genesis of silica-undersaturated ocean island lavas. *Journal of Petrology* **47**, 647–671, doi:10.1093/petrology/egi088.

Dasgupta, R., Hirschmann, M. M. & Smith, N. D. (2007). Partial melting experiments of peridotite $+ CO_2$ at 3 GPa and genesis of alkalic ocean island basalts. *Journal of Petrology* **48**, 2093–2124, doi:10.1093/petrology/egm053.

Dasgupta, R., Jackson, M. G. & Lee, C.-T. A. (2010). Major element chemistry of ocean island basalts—conditions of mantle melting and heterogeneity of mantle source. *Earth and Planetary Science Letters* **289**, 377–392.

Dasgupta, R., Mallik, A., Tsuno, K., Withers, A. C., Hirth, G. & Hirschmann, M. M. (2013). Carbon-dioxide-rich silicate melt in the Earth's upper mantle. *Nature* **493**, 211–215, doi:10.1038/nature11731.

Dautria, J. M., Dupuy, C., Takherist, D. & Dostal, J. (1992). Carbonate metasomatism in the lithospheric mantle: peridotitic xenoliths from a melilititic district of the Sahara basin.

Contributions to Mineralogy and Petrology **111**, 37–52, doi:10.1007/bf00296576.

Davis, F. A., Tangeman, J. A., Tenner, T. J. & Hirschmann, M. M. (2009). The composition of KLB-1 peridotite. *American Mineralogist* **94**, 176–180, doi:10.2138/am.2009.2984.

Davis, F. A., Hirschmann, M. M. & Humayun, M. (2011). The composition of the incipient partial melt of garnet peridotite at 3 GPa and the origin of OIB. *Earth and Planetary Science Letters* **308**, 380–390.

Dawson, J. B., Smith, J. V. & Steele, I. M. (1995). Petrology and mineral chemistry of plutonic igneous xenoliths from the carbonatite volcano, Oldoinyo Lengai, Tanzania. *Journal of Petrology* **36**, 797–826, doi:10.1093/petrology/36.3.797.

de Ignacio, C., Munoz, M. & Sagredo, J. (2012). Carbonatites and associated nephelinites from São Vicente, Cape Verde Islands. *Mineralogical Magazine* **76**, 311–355, doi:10.1180/minmag.2012.076.2.05.

Delano, J. (1980). Chemistry and liquidus phase relations of Apollo 15 red glass. Implications for the deep lunar interior. *11th Lunar and Planetary Science Conference Houston, TX, March 17–21, Proceedings, Volume 1*, A82-22251 09–91 Pergamon Press, pp. 251–288.

Delpech, G., Gregoire, M., O'Reilly, S. Y., Cottin, J. Y., Moine, B., Michon, G. & Giret, A. (2004). Feldspar from carbonate-rich silicate metasomatism in the shallow oceanic mantle under Kerguelen Islands (South Indian Ocean). *Lithos* **75**, 209–237.

Duprat, H. I., Friis, J., Holm, P. M., Grandvuinet, T. & Sorensen, R. V. (2007). The volcanic and geochemical development of São Nicolau, Cape Verde Islands: Constraints from field and $^{40}Ar/^{39}Ar$ evidence. *Journal of Volcanology and Geothermal Research* **162**, 1–19.

Dyhr, C. T. & Holm, P. M. (2010). A volcanological and geochemical investigation of Boa Vista, Cape Verde Islands; $^{40}Ar/^{39}Ar$ geochronology and field constraints. *Journal of Volcanology and Geothermal Research* **189**, 19–32.

Eggler, D. H. (1978). The effect of CO_2 upon partial melting of peridotite in the system $Na_2O–CaO–Al_2O_3–MgO–SiO_2–CO_2$ to 35 kb, with an analysis of melting in a peridotite–$H_2O–CO_2$ system. *American Journal of Science* **278**, 305–343, doi:10.2475/ajs.278.3.305.

Falloon, T. J. & Green, D. H. (1989). The solidus of carbonated, fertile peridotite. *Earth and Planetary Science Letters* **94**, 364–370, doi:http://dx.doi.org/10.1016/0012-821X(89)90153-2.

Filiberto, J. & Dasgupta, R. (2011). Fe^{2+}–Mg partitioning between olivine and basaltic melts: applications to genesis of olivine-phyric shergottites and conditions of melting in the Martian interior. *Earth and Planetary Science Letters* **304**, 527–537.

Foley, S. F. (2011). A reappraisal of redox melting in the Earth's mantle as a function of tectonic setting and time. *Journal of Petrology* **52**, 1363–1391, doi:10.1093/petrology/egq061.

France, L. & Nicollet, C. (2010). MetaRep, an extended CMAS 3D program to visualize mafic (CMAS, ACF-S, ACF-N) and pelitic (AFM-K, AFM-S, AKF-S) projections. *Computers and Geosciences* **36**, 786–791, doi:10.1016/j.cageo.2010.01.001.

Frey, F. A., Green, D. H. & Roy, S. D. (1978). Integrated models of basalt petrogenesis: a study of quartz tholeiites to olivine melilitites from south eastern Australia utilizing geochemical and experimental petrological data. *Journal of Petrology* **19**, 463–513, doi:10.1093/petrology/19·3·463.

Frost, D. & Wood, B. (1995). Experimental measurements of the graphite C–O equilibrium and CO_2 fugacities at high temperature and pressure. *Contributions to Mineralogy and Petrology* **121**, 303–308, doi:10.1007/bf02688245.

Gerbode, C. & Dasgupta, R. (2010). Carbonate-fluxed melting of MORB-like pyroxenite at 2·9 GPa and genesis of HIMU ocean island basalts. *Journal of Petrology* **51**, 2067–2088, doi:10.1093/petrology/egq049.

Grassi, D. & Schmidt, M. W. (2011). The melting of carbonated pelites from 70 to 700 km depth. *Journal of Petrology* **52**, 765–789, doi:10.1093/petrology/egr002.

Gregoire, M., Moine, B. N., O'Reilly, S. Y., Cottin, J. Y. & Giret, A. (2000). Trace element residence and partitioning in mantle xenoliths metasomatized by highly alkaline, silicate- and carbonate-rich melts (Kerguelen Islands, Indian Ocean). *Journal of Petrology* **41**, 477–509, doi:10.1093/petrology/41.4.477.

Guillot, B. & Sator, N. (2011). Carbon dioxide in silicate melts: A molecular dynamics simulation study. *Geochimica et Cosmochimica Acta* **75**, 1829–1857.

Hammouda, T. (2003). High-pressure melting of carbonated eclogite and experimental constraints on carbon recycling and storage in the mantle. *Earth and Planetary Science Letters* **214**, 357–368.

Hammouda, T. & Laporte, D. (2000). Ultrafast mantle impregnation by carbonatite melts. *Geology* **28**, 283–285, doi:10.1130/0091-7613(2000)28<283:umibcm>2.0.co;2.

Heaman, L. M., Creaser, R. A. & Cookenboo, H. O. (2002). Extreme enrichment of high field strength elements in Jericho eclogite xenoliths: A cryptic record of Paleoproterozoic subduction, partial melting, and metasomatism beneath the Slave craton, Canada. *Geology* **30**, 507–510, doi:10.1130/0091-7613(2002)030<0507:eeohfs>2.0.co;2.

Hegner, E., Walter, H. J. & Satir, M. (1995). Pb–Sr–Nd isotopic compositions and trace element geochemistry of megacrysts and melilitites from the Tertiary Urach volcanic field: source composition of small volume melts under SW Germany. *Contributions to Mineralogy and Petrology* **122**, 322–335, doi:10.1007/s004100050131.

Herzberg, C., Gasparik, T. & Sawamoto, H. (1990). Origin of mantle peridotite: Constraints from melting experiments to 16·5 GPa. *Journal of Geophysical Research: Solid Earth* **95**, 15779–15803, doi:10.1029/JB095iB10p15779.

Hirose, K. (1997). Partial melt compositions of carbonated peridotite at 3 GPa and role of CO_2 in alkali-basalt magma generation. *Geophysical Research Letters* **24**, 2837–2840, doi:10.1029/97gl02956.

Hirose, K. & Kushiro, I. (1993). Partial melting of dry peridotites at high pressures: determination of compositions of melts segregated from peridotite using aggregates of diamond. *Earth and Planetary Science Letters* **114**, 477–489.

Ho, K.-s., Chen, J.-c., Lo, C.-h. & Zhao, H.-l. (2003). $^{40}Ar–^{39}Ar$ dating and geochemical characteristics of late Cenozoic basaltic rocks from the Zhejiang–Fujian region, SE China: eruption ages, magma evolution and petrogenesis. *Chemical Geology* **197**, 287–318.

Hofmann, A. W. (1988). Chemical differentiation of the Earth: the relationship between mantle, continental crust, and oceanic crust. *Earth and Planetary Science Letters* **90**, 297–314.

Hofmann, A. W. (1997). Mantle geochemistry: the message from oceanic volcanism. *Nature* **385**, 219–229.

Hofmann, A. W. & White, W. M. (1982). Mantle plumes from ancient oceanic crust. *Earth and Planetary Science Letters* **57**, 421–436.

Ionov, D. A., O'Reilly, S. Y., Genshaft, Y. S. & Kopylova, M. G. (1996). Carbonate-bearing mantle peridotite xenoliths from Spitsbergen: phase relationships, mineral compositions and trace-element residence. *Contributions to Mineralogy and Petrology* **125**, 375–392, doi:10.1007/s004100050229.

Ivanikov, V. V., Rukhlov, A. S. & Bell, K. (1998). Magmatic evolution of the melilitite–carbonatite–nephelinite dyke series of the Turiy Peninsula (Kandalaksha Bay, White Sea, Russia). *Journal of Petrology* **39**, 2043–2059, doi:10.1093/petroj/39.11-12.2043.

Jackson, M. G. & Dasgupta, R. (2008). Compositions of HIMU, EM1, and EM2 from global trends between radiogenic isotopes and major elements in ocean island basalts. *Earth and Planetary Science Letters* **276**, 175–186.

Janney, P. E., Le Roex, A. P., Carlson, R. W. & Viljoen, K. S. (2002). A chemical and multi-isotope study of the Western Cape Olivine Melilitite Province, South Africa: implications for the sources of kimberlites and the origin of the HIMU signature in Africa. *Journal of Petrology* **43**, 2339–2370, doi:10.1093/petrology/43.12.2339.

Kamenetsky, M. B., Sobolev, A. V., Kamenetsky, V. S., Maas, R., Danyushevsky, L. V., Thomas, R., Pokhilenko, N. P. & Sobolev, N. V. (2004). Kimberlite melts rich in alkali chlorides and carbonates: A potent metasomatic agent in the mantle. *Geology* **32**, 845–848, doi:10.1130/g20821.1.

Kawabata, H., Hanyu, T., Chang, Q., Kimura, J.-I., Nichols, A. R. L. & Tatsumi, Y. (2011). The petrology and geochemistry of St. Helena alkali basalts: evaluation of the oceanic crust-recycling model for HIMU OIB. *Journal of Petrology* **52**, 791–838, doi:10.1093/petrology/egr003.

Kiseeva, E. S., Yaxley, G. M., Hermann, J., Litasov, K. D., Rosenthal, A. & Kamenetsky, V. S. (2012). An experimental study of carbonated eclogite at 3·5–5·5 GPa—implications for silicate and carbonate metasomatism in the cratonic mantle. *Journal of Petrology* **53**, 727–759, doi:10.1093/petrology/egr078.

Kogiso, T., Hirose, K. & Takahashi, E. (1998). Melting experiments on homogeneous mixtures of peridotite and basalt: application to the genesis of ocean island basalts. *Earth and Planetary Science Letters* **162**, 45–61.

Koster van Groos, A. F. & Wyllie, P. J. (1966). Liquid immiscibility in the system $Na_2O–Al_2O_3–SiO_2–CO_2$ at pressures to 1 kilobar. *American Journal of Science* **264**, 234–255, doi:10.2475/ajs.264.3.234.

Kushiro, I. (1975). On the nature of silicate melt and its significance in magma genesis; regularities in the shift of the liquidus boundaries involving olivine, pyroxene, and silica minerals. *American Journal of Science* **275**, 411–431, doi:10.2475/ajs.275.4.411.

Kushiro, I. & Walter, M. J. (1998). Mg–Fe partitioning between olivine and mafic–ultramafic melts. *Geophysical Research Letters* **25**, 2337–2340, doi:10.1029/98gl01844.

Lambart, S., Laporte, D., Provost, A. & Schiano, P. (2012). Fate of pyroxenite-derived melts in the peridotitic mantle: thermodynamic and experimental constraints. *Journal of Petrology* **53**, 451–476, doi:10.1093/petrology/egr068.

Lassiter, J. C. & Hauri, E. H. (1998). Osmium-isotope variations in Hawaiian lavas: evidence for recycled oceanic lithosphere in the Hawaiian plume. *Earth and Planetary Science Letters* **164**, 483–496.

Le Bas, M. J. (1989). Nephelinitic and basanitic rocks. *Journal of Petrology* **30**, 1299–1312, doi:10.1093/petrology/30.5.1299.

Lee, W.-J. & Wyllie, P. J. (1997). Liquid immiscibility in the join $NaAlSiO_4–NaAlSi_3O_8–CaCO_3$ at 1 GPa: implications for crustal carbonatites. *Journal of Petrology* **38**, 1113–1135, doi:10.1093/petroj/38.9.1113.

Litasov, K. & Ohtani, E. (2010). The solidus of carbonated eclogite in the system $CaO–Al_2O_3–MgO–SiO_2–Na_2O–CO_2$ to 32 GPa and carbonatite liquid in the deep mantle. *Earth and Planetary Science Letters* **295**, 115–126, doi:10.1016/j.epsl.2010.03.030.

Longhi, J. (2002). Some phase equilibrium systematics of lherzolite melting: I. *Geochemistry, Geophysics, Geosystems* **3**, 1020, doi:10.1029/2001gc000204.

Mallik, A. & Dasgupta, R. (2012). Reaction between MORB-eclogite derived melts and fertile peridotite and generation of ocean island basalts. *Earth and Planetary Science Letters* **329–330**, 97–108.

Martins, S., Mata, J., Munhá, J., Mendes, M., Maerschalk, C., Caldeira, R. & Mattielli, N. (2010). Chemical and mineralogical evidence of the occurrence of mantle metasomatism by carbonate-rich melts in an oceanic environment (Santiago Island, Cape Verde). *Mineralogy and Petrology* **99**, 43–65, doi:10.1007/s00710-009-0078-x.

Matzen, A. K., Baker, M. B., Beckett, J. R. & Stolper, E. M. (2011). Fe–Mg partitioning between olivine and high-magnesian melts and the nature of Hawaiian parental liquids. *Journal of Petrology*, doi:10.1093/petrology/egq089.

Medard, E., McCammon, C. A., Barr, J. A. & Grove, T. L. (2008). Oxygen fugacity, temperature reproducibility, and H_2O contents of nominally anhydrous piston-cylinder experiments using graphite capsules. *American Mineralogist* **93**, 1838–1844, doi:10.2138/am.2008.2842.

Melluso, L., le Roex, A. P. & Morra, V. (2011). Petrogenesis and Nd-, Pb-, Sr-isotope geochemistry of the Cenozoic olivine melilitites and olivine nephelinites ('ankaratrites') in Madagascar. *Lithos* **127**, 505–521.

Minarik, W. G. & Watson, E. B. (1995). Interconnectivity of carbonate melt at low melt fraction. *Earth and Planetary Science Letters* **133**, 423–437, doi:10.1016/0012-821X(95)00085-Q.

Mollo, S., Gaeta, M., Freda, C., Di Rocco, T., Misiti, V. & Scarlato, P. (2010). Carbonate assimilation in magmas: a reappraisal based on experimental petrology. *Lithos* **114**, 503–514, doi:10.1016/j.lithos.2009.10.013.

Mourão, C., Mata, J., Doucelance, R., Madeira, J., da Silveira, A. B., Silva, L. C. & Moreira, M. (2010). Quaternary extrusive calciocarbonatite volcanism on Brava Island (Cape Verde): a nephelinite–carbonatite immiscibility product. *Journal of African Earth Sciences* **56**, 59–74.

Mysen, B. O., Arculus, R. J. & Eggler, D. H. (1975). Solubility of carbon dioxide in melts of andesite, tholeiite, and olivine nephelinite composition to 30 kbar pressure. *Contributions to Mineralogy and Petrology* **53**, 227–239, doi:10.1007/BF00382441.

Nielsen, T. F. D., Solovova, I. P. & Veksler, I. V. (1997). Parental melts of melilitolite and origin of alkaline carbonatite: evidence from crystallised melt inclusions, Gardiner complex. *Contributions to Mineralogy and Petrology* **126**, 331–344, doi:10.1007/s004100050254.

O'Hara, M. J. (1968). The bearing of phase equilibria studies in synthetic and natural systems on the origin and evolution of basic and ultrabasic rocks. *Earth-Science Reviews* **4**, 69–133.

O'Hara, M. J. & Yoder, H. S. (1967). Formation and fractionation of basic magmas at high pressures. *Scottish Journal of Geology* **3**, 67–117.

Perkins, P. (2006). smoothhist2D: smoothhist2D(X, lambda, nbins, outliercutoff, plottype) File Exchange. MATLAB Central http://www.mathworks.com/matlabcentral/fileexchange/13352-smooth-hist2d/content/smoothhist2D.m.

Pertermann, M. & Hirschmann, M. M. (2003). Anhydrous partial melting experiments on MORB-like eclogite: phase relations, phase compositions and mineral–melt partitioning of major elements at 2–3 GPa. *J. Petrology* **44**, 2173–2201, doi:10.1093/petrology/egg074.

Pilet, S., Hernandez, J. & Villemant, B. (2002). Evidence for high silicic melt circulation and metasomatic events in the mantle beneath alkaline provinces: the Na–Fe-augitic green-core pyroxenes in the Tertiary alkali basalts of the Cantal massif (French Massif Central). *Mineralogy and Petrology* **76**, 39–62, doi:10.1007/s007100200031.

Prytulak, J. & Elliott, T. (2007). TiO_2 enrichment in ocean island basalts. *Earth and Planetary Science Letters* **263**, 388–403.

Raddick, M. J., Parmentier, E. M. & Scheirer, D. S. (2002). Buoyant decompression melting: a possible mechanism for intraplate volcanism. *Journal of Geophysical Research: Solid Earth* **107**, ECV 7-1–ECV 7-14, doi:10.1029/2001jb000617.

Ravna, K. (2000). The garnet–clinopyroxene Fe^{2+}–Mg geothermometer: an updated calibration. *Journal of Metamorphic Geology* **18**, 211–219, doi:10.1046/j.1525-1314.2000.00247.x.

Roeder, P. L. & Emslie, R. F. (1970). Olivine–liquid equilibrium. *Contributions to Mineralogy and Petrology* **29**, 275–289, doi:10.1007/bf00371276.

Rohrbach, A., Ballhaus, C., Golla-Schindler, U., Ulmer, P., Kamenetsky, V. S. & Kuzmin, D. V. (2007). Metal saturation in the upper mantle. *Nature* **449**, 456–458, doi:10.1038/nature06183.

Rohrbach, A., Ballhaus, C., Ulmer, P., Golla-Schindler, U. & Schönbohm, D. (2011). Experimental evidence for a reduced metal-saturated upper mantle. *Journal of Petrology* **52**, 717–731, doi:10.1093/petrology/egq101.

Schultz, F., Lehmann, B., Tawackoli, S., Rössling, R., Belyatsky, B. & Dulski, P. (2004). Carbonatite diversity in the Central Andes: the Ayopaya alkaline province, Bolivia. *Contributions to Mineralogy and Petrology* **148**, 391–408, doi:10.1007/s00410-004-0612-0.

Shcheka, S. S., Wiedenbeck, M., Frost, D. J. & Keppler, H. (2006). Carbon solubility in mantle minerals. *Earth and Planetary Science Letters* **245**, 730–742, doi:10.1016/j.epsl.2006.03.036.

Spandler, C., Yaxley, G., Green, D. H. & Rosenthal, A. (2008). Phase relations and melting of anhydrous K-bearing eclogite from 1200 to 1600°C and 3 to 5 GPa. *Journal of Petrology* **49**, 771–795, doi:10.1093/petrology/egm039.

Spera, F. J. (1981). Carbon dioxide in igneous petrogenesis: II. Fluid dynamics of mantle metasomatism. *Contributions to Mineralogy and Petrology* **77**, 56–65, doi:10.1007/bf01161502.

Stagno, V. & Frost, D. J. (2010). Carbon speciation in the asthenosphere: experimental measurements of the redox conditions at which carbonate-bearing melts coexist with graphite or diamond in peridotite assemblages. *Earth and Planetary Science Letters* **300**, 72–84.

Stagno, V., Ojwang, D. O., McCammon, C. A. & Frost, D. J. (2013). The oxidation state of the mantle and the extraction of carbon from Earth's interior. *Nature* **493**, 84–88, doi:10.1038/nature11679.

Stixrude, L. & Lithgow-Bertelloni, C. (2012). Geophysics of chemical heterogeneity in the mantle. *Annual Review of Earth and Planetary Sciences* **40**, 569–595, doi:10.1146/annurev.earth.36.031207.124244.

Takahashi, E. (1986). Melting of a dry peridotite KLB-1 up to 14 GPa: implications on the origin of peridotitic upper mantle. *Journal of Geophysical Research* **91**, 9367–9382, doi:10.1029/JB091iB09p09367.

Takamasa, A., Nakai, S. i., Sahoo, Y., Hanyu, T. & Tatsumi, Y. (2009). W isotope compositions of oceanic islands basalts from French Polynesia and their meaning for core–mantle interaction. *Chemical Geology* **260**, 37–46.

Torres, P., Silva, L. C., Munhá, J., Caldeira, R., Mata, J. & Tassinari, C. (2010). Petrology and Geochemistry of lavas from Sal Island: Implications for the variability of the Cape Verde magmatism. *Comunicações Geológicas* **97**, 35–62.

Tschegg, C., Ntaflos, T. & Akinin, V. V. (2011). Polybaric petrogenesis of Neogene alkaline magmas in an extensional tectonic environment: Viliga Volcanic Field, northeast Russia. *Lithos* **122**, 13–24.

Tsuno, K. & Dasgupta, R. (2011). Melting phase relation of nominally anhydrous, carbonated pelitic-eclogite at 2·5–3·0 GPa and deep cycling of sedimentary carbon. *Contributions to Mineralogy and Petrology* **161**, 743–763, doi:10.1007/s00410-010-0560-9.

Tsuno, K., Dasgupta, R., Danielson, L. & Righter, K. (2012). Flux of carbonate melt from deeply subducted pelitic sediments: Geophysical and geochemical implications for the source of Central American volcanic arc. *Geophysical Research Letters* **39**, L16307, doi:10.1029/2012GL052606.

Wagner, T. P. & Grove, T. L. (1997). Experimental constraints on the origin of lunar high-Ti ultramafic glasses. *Geochimica et Cosmochimica Acta* **61**, 1315–1327, doi:10.1016/S0016-7037(96)00387-0.

Walter, M. J. (1998). Melting of garnet peridotite and the origin of komatiite and depleted lithosphere. *Journal of Petrology* **39**, 29–60.

Wendlandt, R. F. & Mysen, B. O. (1980). Melting phase relations of natural peridotite + CO_2 as a function of degree of partial melting at 15 and 30 kbar. *American Mineralogist* **65**, 37–44.

Wilson, M., Rosenbaum, J. M. & Dunworth, E. A. (1995). Melilitites: partial melts of the thermal boundary layer? *Contributions to Mineralogy and Petrology* **119**, 181–196, doi:10.1007/bf00307280.

Wyllie, P. J. (1978). Mantle fluid compositions buffered in peridotite—by carbonates, amphibole, and phlogopite. *Journal of Geology* **86**, 687–713.

Wyllie, P. J. & Huang, W. L. (1976). High CO_2 solubilities in mantle magmas. *Geology* **4**, 21–24, doi:10.1130/0091-7613(1976)4<21:hcsimm>2.0.co;2.

Xirouchakis, D., Hirschmann, M. M. & Simpson, J. A. (2001). The effect of titanium on the silica content and on mineral–liquid partitioning of mantle-equilibrated melts. *Geochimica et Cosmochimica Acta* **65**, 2201–2217.

Yasuda, A., Fujii, T. & Kurita, K. (1994). Melting phase relations of an anhydrous mid-ocean ridge basalt from 3 to 20 GPa: Implications for the behavior of subducted oceanic crust in the mantle. *Journal of Geophysical Research* **99**, 9401–9414, doi:10.1029/93jb03205.

Yaxley, G. & Brey, G. (2004). Phase relations of carbonate-bearing eclogite assemblages from 2·5 to 5·5 GPa: implications for petrogenesis of carbonatites. *Contributions to Mineralogy and Petrology* **146**, 606–619, doi:10.1007/s00410-003-0517-3.

Yaxley, G. & Green, D. (1998). Reactions between eclogite and peridotite: mantle refertilisation by subduction of oceanic crust. *Schweizerische Mineralogische und Petrographische Mitteilungen* **78**, 243–255.

Yaxley, G. M., Green, D. H. & Kamenetsky, V. (1998). Carbonatite metasomatism in the southeastern Australian lithosphere. *Journal of Petrology* **39**, 1917–1930, doi:10.1093/petroj/39.11-12.1917.

Zeng, G., Chen, L.-H., Xu, X.-S., Jiang, S.-Y. & Hofmann, A. W. (2010). Carbonated mantle sources for Cenozoic intra-plate alkaline basalts in Shandong, North China. *Chemical Geology* **273**, 35–45.

Zindler, A. & Hart, S. (1986). Chemical geodynamics. *Annual Review of Earth and Planetary Sciences* **14**, 493–571.